Inorg. Chem. **2002**, *41*, 5005–5023

Synthesis and Characterization of Volatile, Fluorine-Free β-Ketoiminate Lanthanide MOCVD Precursors and Their Implementation in Low-Temperature Growth of Epitaxial CeO_2 Buffer Layers for Superconducting Electronics

Nikki L. Edleman,[†] Anchuan Wang,[†] John A. Belot,[†] Andrew W. Metz,[†] Jason R. Babcock,[†] Amber M. Kawaoka,[†] Jun Ni,[†] Matthew V. Metz,[†] Christine J. Flaschenriem,[†] Charlotte L. Stern,[†] Louise M. Liable-Sands,[‡] Arnold L. Rheingold,[‡] Paul R. Markworth,[§] Robert P. H. Chang,[§] Michael P. Chudzik,[||] Carl R. Kannewurf,[||] and Tobin J. Marks*,[†]

Department of Chemistry and the Materials Research Center, Northwestern University, Evanston, Illinois 60208, Department of Chemistry and Biochemistry, University of Delaware, Newark, Delaware 19716, Department of Materials Science and the Materials Research Center, Northwestern University, Evanston, Illinois 60208, and Department of Electrical and Computer Engineering and the Materials Research Center, Northwestern University, Evanston, Illinois 60208

Received April 29, 2002

A new class of volatile, low-melting, fluorine-free lanthanide metal–organic chemical vapor deposition (MOCVD) precursors has been developed. The neutral, monomeric Ce, Nd, Gd, and Er complexes are coordinatively saturated by a versatile, multidentate ether-functionalized β-ketoiminato ligand series, the melting point and volatility characteristics of which can be tuned by altering the alkyl substituents on the keto, imino, and ether sites of the ligand. Direct comparison with conventional lanthanide β-diketonate complexes reveals that the present precursor class is a superior choice for lanthanide oxide MOCVD. Epitaxial CeO_2 buffer layer films can be grown on (001) YSZ substrates by MOCVD at significantly lower temperatures (450–650 °C) than previously possible by using one of the newly developed cerium β-ketoiminate precursors. Films deposited at 540 °C have good out-of-plane ($\Delta\omega = 0.85°$) and in-plane ($\Delta\phi = 1.65°$) alignment and smooth surfaces (rms roughness $\sim$ 4.3 Å). The film growth rate decreases and the films tend to be smoother as the deposition temperature is increased. High-quality yttrium barium copper oxide (YBCO) films grown on these CeO_2 buffer layers by pulsed organometallic molecular beam epitaxy exhibit very good electrical transport properties ($T_c = 86.5$ K, $J_c = 1.08 \times 10^6$ A/cm^2 at 77.4 K).

Introduction

The growth and properties of lanthanide-containing oxide films is of great current interest to the chemistry, materials science, and electronics communities.[1−4] Applications include multilayer device buffer layers (e.g., CeO_2),[5−12] high dielectric constant (high-*k*) materials (e.g., Gd_2O_3),[13,14] high-

* To whom correspondence should be addressed. E-mail: t-marks@northwestern.edu.

[†] Department of Chemistry and the Materials Research Center, Northwestern University.

[‡] Department of Chemistry and Biochemistry, University of Delaware.

[§] Department of Materials Science and the Materials Research Center.

[||] Department of Electrical and Computer Engineering and the Materials Research Center.

(1) Bunzli, J.-C. G.; Andre, N.; Elhabiri, M.; Muller, G.; Piquet, C. *J. Alloys Compd.* **2000**, *303−304*, 66−74.
(2) Tiitta, M.; Niinisto, L. *Chem. Vap. Deposition* **1997**, *3*, 167−182.
(3) Gun'ko, Y. K.; Edelmann, F. T. *Comments Inorg. Chem.* **1997**, *19*, 153−184.
(4) Lewkebandara, T. S.; Winter, C. H. *Chemtracts: Inorg. Chem.* **1994**, 271−282.
(5) Jimenez, C.; Weiss, F.; Senateur, J. P.; Abrutis, A.; Krellmann, M.; Selbmann, D.; Eickemeyer, J.; Stadel, O.; Wahl, G. *IEEE Trans. Appl. Supercond.* **2001**, *11*, 2905−2908.
(6) Selvamanickam, V.; Carota, G.; Funk, M.; Vo, N.; Haldar, P.; Balachandran, Y.; Chudzik, M.; Arendt, P.; Groves, J. R.; DePaula, R.; Newnam, B. *IEEE Trans. Appl. Supercond.* **2001**, *11*, 3379−3381.
(7) Knierim, A.; Auer, R.; Geerk, J.; Linker, G.; Meyer, O.; Reiner, H.; Schneider, R. *Appl. Phys. Lett.* **1997**, *70*, 661−663.
(8) Norton, D. P.; Goyal, A.; Budai, J. D.; Christen, D. K.; Kroeger, D. M.; Specht, E. D.; He, Q.; Saffian, B.; Paranthaman, M.; Klabunde, C. E.; Lee, D. F.; Sales, B. C.; List, F. A. *Science* **1996**, *274*, 755−757.
(9) Philips, J. M. *J. Appl. Phys.* **1996**, *79*, 1829−1848.
(10) Suzuki, M.; Ami, T. *Mater. Sci. Eng.* **1996**, *B41*, 166−173.

10.1021/ic020299h CCC: $22.00
Published on Web 09/10/2002

temperature superconductors (e.g., $LnBa_2Cu_3O_{7-\delta}$),[15−17] phosphor dopants,[18−21] solid-state oxide fuel cells,[22] and magnetic materials.[23]

MOCVD (metal−organic chemical vapor deposition) offers many attractions for oxide film growth, including low equipment costs, straightforward scale-up, conformal deposition on a variety of complex substrates, low growth temperatures, and rapid growth rates. However, the success of an MOCVD process depends critically on the availability of volatile, thermally stable precursors which exhibit constant vapor pressure and the capacity to selectively form the desired phase at the substrate surface. Low-melting precursors are preferred because solid compounds can be handled with ease at room temperature, while the liquid form at reservoir operating temperatures affords constant surface area for stable vapor delivery to the reactor.[24−32]

The design and realization of new molecular MOCVD precursors offers a considerable synthetic challenge. For many applications, the metal ion of interest is of large ionic radius and therefore has many coordination sites which require saturation to prevent volatility-depressing oligomerization. Large ion size is often further complicated by a low ionic charge, demanding the use of multidentate anionic and/or donating ligands in order to ensure a monomeric, neutrally charged metal complex.[33,34] In addition, the use of metal−carbon bonded ligand frameworks (e.g., substituted cyclopentadienyls[35]) or fluorinated ligand substituents[22,36] often leads to impurity incorporation which compromises desired film properties.[37,38]

No known lanthanide precursor satisfies all of the above criteria, although the extensive body of known lanthanide complexes[39−42] offers many potential candidates to the synthetic chemist. A common structural motif employs nonfluorinated β-diketonate ligands (**I**). Metal−organic

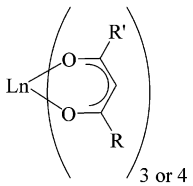

R, R' = alkyl group

I

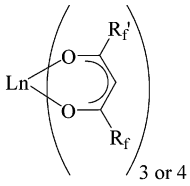

R_f, R_f' = perfluorinated alkyl group

II

complexes such as **I** suffer falling volatility over film growth times due to oligomerization, thermal decomposition, and sintering.[22,36,43−45] In addition, these sources frequently require undesirably high growth temperatures.[36,46,47] The volatilization temperature of type **I** precursors must often be continuously ramped in order to provide a constant precursor vapor pressure in the film growth reactor.[48] β-Diketonate precursor volatility and thermal stability have been improved by the use of fluorinated ligand substituents (**II**); however, formation of fluoride phases in the resulting films is problematic,[22] and F^- species can corrode certain (i.e., metal) substrates and reactor components.[49]

A major research effort has focused on the synthesis of alternative precursors for lanthanide oxide MOCVD with the goal of overcoming the difficulties associated with common sources as described above. Lanthanide tris[bis(trimethylsilyl)amides] (**III**) have been used (primarily for ALE),[50−52]

(11) Van Wijck, M. A. A. M.; Verhoeven, M. A. J.; Reuvekamp, E. M. C. M.; Gerritsma, G. J.; Blank, D. H. A.; Rogalla, H. *Appl. Phys. Lett.* **1996**, *68*, 553−555.
(12) Schulz, D. L.; Marks, T. J. *Adv. Mater.* **1994**, *6*, 719−730.
(13) Kwo, J.; Hong, M.; Kortan, A. R.; Queeney, K. L.; Chabal, Y. J.; Opila, R. L., Jr.; Muller, D. A.; Chu, S. N. G.; Sapjeta, B. J.; Lay, T. S.; Mannaerts, J. P.; Boone, T.; Krautter, H. W.; Krajewski, J. J.; Sergent, A. M.; Rosamilia, J. M. *J. Appl. Phys.* **2001**, *89*, 3920−3927.
(14) Hong, M.; Kwo, J.; Kortan, A. R.; Mannaerts, J. P.; Sergent, A. M. *Science* **1999**, *283*, 1897−1900.
(15) Rosner, C. H. *IEEE Trans. Appl. Supercond.* **2001**, *11*, 39−48.
(16) Norton, D. P. *Annu. Rev. Mater. Sci.* **1998**, *28*, 299−343.
(17) Macmanus-Driscoll, J. L. *Adv. Mater.* **1997**, *9*, 457−473.
(18) Kushida, T. *Springer Series Solid-State Sci.* **2000**, *128*, 1−35.
(19) Teren, A. R.; Wessels, B. W. *Mater. Res. Soc. Symp. Proc.* **2000**, *597*, 15−20.
(20) Rack, P. D.; Naman, A.; Holloway, P. H.; Sun, S. S.; Tuenge, R. T. *MRS Bull.* **1996**, *21*, 49−58.
(21) Ronda, C. R.; Justel, T.; Nikol, H. *J. Alloys Compd.* **1998**, *277*, 669−676.
(22) McAleese, J.; Plakatouras, J. C.; Steele, B. C. H. *Thin Solid Films* **1996**, *280*, 152−159.
(23) Collocott, S. J.; Dunlop, J. B.; Lovatt, H. C.; Ramsden, V. S. *Mater. Sci. Forum* **1999**, *315*−*317*, 77−83.
(24) Lindler, J.; Schumacher, M.; Dauelsberg, M.; Schienle, F.; Miedl, S.; Burgess, D.; Merz, E.; Strauch, G.; Juergensen, H. *Adv. Mater. Opt. Electron.* **2000**, *10*, 163−167.
(25) Gleizes, A. N. *Chem. Vap. Deposition* **2000**, *6*, 155−173.
(26) Hinds, B. J.; McNeely, R. J.; Studebaker, D. L.; Marks, T. J.; Hogan, T. P.; Schindler, J. L.; Kannewurf, C. R.; Zhang, X. F.; Miller, D. *J. Mater. Res.* **1997**, *12*, 1214−1236.
(27) Marks, T. J.; Belot, J. A.; Reedy, C. J.; McNeely, R. J.; Studebaker, D. L.; Neumayer, D. A.; Stern, C. L. *J. Alloys Compd.* **1997**, *251*, 243−252.
(28) Rees, W. S., Jr., Ed. *CVD of Nonmetals*; VCH Publishers: Weinheim, Germany, 1996.
(29) Kodas, T.; Hampden-Smith, M. *The Chemistry Of Metal CVD*; VCH Publishers: Weinheim, Germany, 1994.
(30) Wessels, B. W. *Annu. Rev. Mater. Sci.* **1995**, *25*, 525−546.
(31) Dahmen, K. H.; Gerfin, T. *Prog. Cryst. Growth Charact. Mater.* **1993** *27*, 117−161.
(32) Marks, T. J. *Pure Appl. Chem.* **1995**, *67*, 313−318.
(33) Belot, J. A.; Neumayer, D. A.; Reedy, C. J.; Studebaker, D. B.; Hinds, B. J.; Stern, C. L.; Marks, T. J. *Chem. Mater.* **1997**, *9*, 1638−1648.
(34) Babcock, J. R.; Benson, D. D.; Wang, A.; Edleman, N. L.; Belot, J. A.; Metz, M. V.; Marks, T. J. *Chem. Vap. Deposition* **2000**, *6*, 180−183.
(35) Nukeaw, J.; Tanagisawa, J.; Matsubara, N.; Fujiwara, Y.; Takeda, Y. *Appl. Phys. Lett.* **1997**, *70*, 84−86.
(36) Becht, M.; Gerfin, T.; Dahmen, K. H. *Chem. Mater.* **1993**, *5*, 137−144.
(37) Greenwald, A. C.; Rees, W. S., Jr.; Lay, U. W. *Mater. Res. Soc. Symp. Proc.* **1993**, *301*, 21−26.
(38) Schmaderer, F.; Huber, R.; Oetzmann, H.; Wahl, G. *Appl. Surf. Sci.* **1990**, *46*, 53−60.
(39) Anwander, R.; Hermann, W. A. *Top. Curr. Chem.* **1996**, *179*, 2−32.
(40) Anwander, R. *Top. Curr. Chem.* **1996**, *179*, 33−112.
(41) Anwander, R. *Top. Curr. Chem.* **1996**, *179*, 149−244.
(42) Joshi, K. C.; Pathak, V. N. *Coord. Chem. Rev.* **1977**, *22*, 37−122.
(43) Graboy, I. E.; Markov, N. V.; Maleev, V. V.; Kaul, A. R.; Polyakov, S. N.; V. L. Svetchnikov, V. L.; Zandbergen, H. W.; Dahmen, K. H. *J. Alloys Compd.* **1997**, *251*, 318−321.
(44) Ikegawa, S.; Motoi, Y. *Thin Solid Films* **1996**, *281*−*282*, 60−63.
(45) Hiskes, R.; DiCarolis, S. A.; Jacowitz, R. D.; Lu, Z.; Fiegelson, R. S.; Ronte, R. K.; Young, J. L. *J. Cryst. Growth* **1993**, *128*, 781−787.
(46) Becht, M.; Wang, F.; Wen, J. G.; Morishita, T. *J. Cryst. Growth* **1997**, *170*, 799−802.
(47) Lu, Z.; Hiskes, R.; DiCarolis, S. A.; Nel, A.; Ronte, R. K.; Fiegelson, R. S. *J. Cryst. Growth* **1995**, *156*, 227−234.
(48) Liang, S.; Chern, C. S.; Shi, Z. Q.; Lu, P.; Lu, Y.; Kear, B. H. *J. Cryst. Growth* **1995**, *151*, 359−364.
(49) Chadwick, D.; McAleese, J.; Senkiw, K.; Steele, B. C. H. *Appl. Surf. Sci.* **1996**, *99*, 417−420.
(50) Gordon, R. G.; Becker, J.; Hausmann, D.; Suh, S. *Chem. Mater.* **2001**, *13*, 2463−2464.

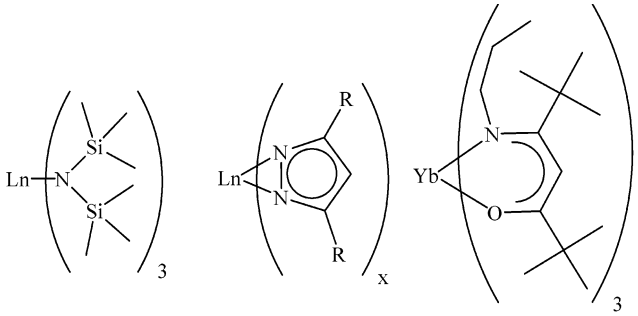

III **IV** **V**

although the working lifetime of these materials is limited by the appreciable air-sensitivity. Winter and co-workers have developed a series of complexes with pyrazolato ligand systems (**IV**);[53] however, these compounds have been used only to dope GaAs semiconductor films and have not been demonstrated in pure oxide deposition.[54−56] Rees et al. recently communicated the synthesis of a bidentate *β*-ketoiminato Yb complex (**V**).[57] However, thermogravimetric analysis (TGA) data show that this complex volatilizes at rather high temperatures (∼600 °C), and no film growth using **V** has been reported.

Other groups have made significant synthetic advances in developing classes of lanthanide precursors based on a combined *β*-diketonate + glyme ligation approach. This synthetic strategy was originally demonstrated for alkaline earth compounds[33,58] and is successful because the addition of a donating polyether chain leads to monomeric complexes, in contrast to the parent *β*-diketonates. Several groups have detailed the synthesis of nonfluorinated Ln(*β*-diketonate)$_3$-(glyme) compounds (**VI**),[59−62] although structural data show that, in some cases, the glyme ligand bridges two metal centers, and decomposition of these complexes upon heating has been documented,[59,61] as well as the need for high precursor bubbler temperatures and irreproducible precursor delivery rates.[61] Fluorination of the *β*-diketonato skeleton improves the thermal stability of this precursor class

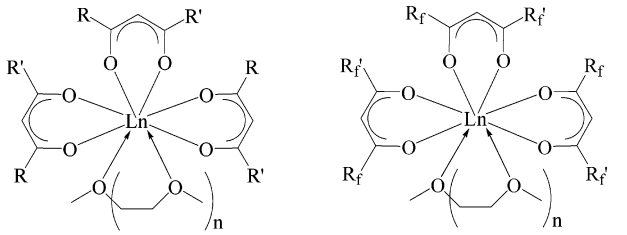

R, R' = alkyl group
n = 1, 2, 3, 5

VI

R_f, R_f' = perfluorinated alkyl group
n = 1, 2, 3, 5

VII

(**VII**),[63−72] although additional processing steps are required to remove and/or prevent fluoride phase formation,[63,68,69] and the threat of metal corrosion by F^- species is again a concern.[73]

The goal of this research effort was to design a multidentate, *fluorine-free* ligand system that would address the general precursor considerations discussed above *and* could successfully be applied to the entire lanthanide series, with trivalent 8-coordinate ionic radii ranging from 1.16 to 0.977 Å (La^{3+}−Lu^{3+}).[74] In addition, a precursor that is a *liquid* at typical reactor operating temperatures would avoid the sintering problem commonly encountered with the above-mentioned solid **I** and **II** sources. Therefore, the synthesis and characterization of low-melting, nonfluorinated lanthanide (Ln = Ce^{3+}, Nd^{3+}, Gd^{3+}, and Er^{3+}) complexes bearing homoleptic multidentate *β*-ketoiminato ligands (**VIII**)

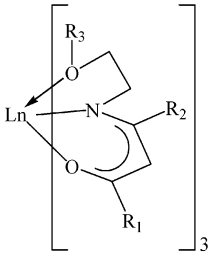

R_1, R_2, R_3 = alkyl

VIII

has been a central goal.[75−78] This ligand system was originally explored by our laboratory for coordinative satura-

(51) Just, O.; Rees, W. S., Jr. *Adv. Mater. Opt. Electron.* **2000**, *10*, 213−221.
(52) Rees, W. S., Jr.; Just, O.; Van Derveer, D. S. *J. Mater. Chem.* **1999**, *9*, 249−252.
(53) Pfeiffer, D.; Ximba, B. J.; Liable-Sands, L. M.; Rheingold, A. L.; Heeg, M. J.; Coleman, D. M.; Schlegel, H. B.; Kuech, T. F.; Winter, C. H. *Inorg. Chem.* **1999**, *38*, 4539−4548.
(54) Cederberg, J. G.; Culp, T. D.; Bieg, B.; Pfeiffer, D.; Winter, C. H.; Bray, K. L.; Kuech, T. F. *J. Appl. Phys.* **1999**, *85*, 1825−1831.
(55) Cederberg, J. G.; Culp, T. D.; Bieg, B.; Pfeiffer, D.; Winter, C. H.; Bray, K. L.; Kuech, T. F. *J. Cryst. Growth* **1998**, *195*, 105−111.
(56) Culp, T. D.; Cederberg, J. G.; Bieg, B.; Kuech, T. F.; Bray, K. L.; Pfeiffer, D.; Winter, C. H. *J. Appl. Phys.* **1998**, *83*, 4918−4927.
(57) Rees, W. S., Jr.; Just, O.; Castro, S. L.; Matthews, J. S. *Inorg. Chem.* **2000**, *39*, 3736−3737.
(58) Teren, A. R.; Belot, J. A.; Edleman, N. L.; Marks, T. J.; Wessels, B. W. *Chem. Vap. Deposition* **2000**, *6*, 175−177.
(59) Drake, S. R.; Lyons, A.; Otway, D. J.; Slawin, A. M. Z.; Williams, D. J. *J. Chem. Soc., Dalton Trans.* **1993**, 2379−2386.
(60) Darr, J. A.; Mingos, D. M. P.; Hibbs, D. E.; Hursthouse, M. B.; Malik, K. M. A. *Polyhedron* **1996**, *15*, 3225−3231.
(61) McAleese, J.; Plakatouras, J. C.; Steele, B. C. H. *Thin Solid Films* **1996**, *286*, 64−71.
(62) Baxter, I.; Drake, S. R.; Hursthouse, M. B.; Malik, K. M. A.; McAleese, J.; Otway, D. J.; Plakatouras, J. C. *Inorg. Chem.* **1995**, *34*, 1384−1394.
(63) McAleese, J.; Darr, J. A.; Steele, B. C. H. *Chem. Vap. Deposition* **1996**, *2*, 244−247.
(64) Baxter, I.; Darr, J. A.; Hursthouse, M. B.; Malik, K. M. A.; McAleese, J.; Mingos, D. M. P. *Polyhedron* **1998**, *17*, 1329−1341.
(65) Malandrino, G.; Bettinelli, M.; Speghini, A.; Fragalà, I. L. *Eur. J. Inorg. Chem.* **2001**, 1039−1044.
(66) (a) Malandrino, G.; Nigro, R. L.; Benelli, C.; Castelli, F.; Fragalà, I. L. *Chem. Vap. Deposition* **2000**, *6*, 233−238. (b) Lo Nigro, R.; Malandrino, G.; Fragalà, I. L. *Chem. Mater.* **2001**, *13*, 4402.
(67) Condorelli, G. G.; Gennaro, S.; Fragalà, I. L. *Chem. Vap. Deposition* **2000**, *6*, 185−192.
(68) Malandrino, G.; Fragalà, I. L. *Chem. Mater.* **1998**, *10*, 3765−3768.
(69) Malandrino, G.; Benelli, C.; Castelli, F.; Fragalà, I. L. *Chem. Mater.* **1998**, *10*, 3434−3444.
(70) Malandrino, G.; Fragalà, I. L.; Aime, S.; Dastru, W.; Gobetto, R.; Benelli, C. *J. Chem. Soc., Dalton Trans.* **1998**, 1509−1512.
(71) Malandrino, G.; Incontro, O.; Castelli, F.; Fragalà, I. L. *Chem. Mater.* **1996**, *8*, 1292−1297.
(72) Malandrino, G.; Licata, R.; Castelli, F.; Fragalà, I. L. *Inorg. Chem.* **1995**, *34*, 6233−6234.
(73) McAleese, J.; Steele, B. C. H. *Corros. Sci.* **1998**, *40*, 113−123.
(74) Shannon, R. D. *Acta Crystallogr.* **1976**, *A32*, 751−767.

tion of alkaline earth ions,[79−82] the MOCVD applications of which offer many of the same challenges as lanthanide ions. A further aim of the present study was to elaborate and investigate the effect of various alkyl substituents at the R_1, R_2, and R_3 sites of ligand **VIII** on precursor melting point and volatility characteristics. In this contribution, lanthanide β-ketoiminate complexes of type **VIII** are named according to the substitution at the R_1, R_2, and R_3 sites, "$Ln(R_1R_2R_3)_3$," and the noncoordinated protonated ligands are simply "$H(R_1R_2R_3)$."

CeO_2, with a cubic fluorite crystal structure (a = 5.411 Å),[83] has been widely investigated as a protective buffer layer for high-temperature superconductor (HTS) films in current-carrying applications[5−9] and as an insulating layer in multilayer electronic devices.[10−12] Compared to YSZ, CeO_2 is a more attractive buffer layer for superconducting $YBa_2Cu_3O_{7-\delta}$ (YBCO) because of the smaller lattice mismatch and similar thermal expansion coefficient. Thus far, many growth techniques including MBE,[84,85] pulsed laser deposition,[86,87] sputtering,[88−90] and electron beam evaporation[91,92] have been utilized for CeO_2 film growth. However, as noted above, molecule-based metal−organic chemical vapor deposition (MOCVD) techniques offer many attractive features such as conformal coverage, ability to coat complex shapes, simplified apparatus, and lower growth temperatures for thin film growth and device fabrication.[24−32] Nevertheless, MOCVD has not been fully optimized for CeO_2 deposition. Although low-temperature film deposition is requisite for multilayer device fabrication, all CeO_2 MOCVD processes reported prior to this contribution have required very high growth temperatures (680−800 °C).[36,46,47,93] Efforts have been made to improve these CeO_2 growth parameters by using special reactors and/or other methods;[48,94] however, high deposition temperatures are still required.

Efficient, reproducible MOCVD CeO_2 growth processes depend crucially on the availability of high-purity metal−organic precursors having high and stable vapor pressures. As discussed above, it has been found that the current generation fluorine-bearing and fluorine-free β-diketonate cerium complexes have inherently poor thermal stability. Some of them [e.g., $Ce(dpm)_4$, dpm = 2,2,6,6-tetramethyl-3,5-heptanedione] decompose within 1 h at temperatures necessary to maintain a useful vapor transport rate. Such high precursor evaporation temperatures (above 200 °C) also present a serious materials complication in MOCVD reactor design(e.g., Teflon components cannot be used). Furthermore, as noted, all of the aforementioned Ce precursors require growth temperatures in excess of 680 °C for high-quality CeO_2 thin film growth, which is undesirable in multilayer device fabrication. In this contribution, we report the first in situ MOCVD deposition of ceria thin films at temperatures as low as 450 °C using one of the newly developed liquid cerium precursors of type **VIII**, and we demonstrate its inherent advantages as a buffer layer for YBCO growth by MOCVD.

Experimental Section

General Synthetic Procedures. All glassware was carefully washed in distilled water (to minimize metal contaminants), rinsed with acetone, and dried for at least 2.0 h in an oven prior to use. Standard Schlenk techniques and either a Vacuum Atmospheres or M. Braun nitrogen-filled glovebox were used in the isolation and handling of all lanthanide reagents and complexes. Diethyl ether and THF solvents were dried over NaK−benzophenone ketyl and distilled immediately prior to use. Pentane and toluene solvents were either dried and distilled from NaK−benzophenone ketyl or passed through a dual-column (alumina and Q-5 copper catalyst) Solvtek solvent purification system. Xylenes were dried over and distilled from molten Na.

Reagents. The reagents 2-methoxyethylamine, pinnacolone, ethyl acetate, ethyl propionate, chlorotrimethylsilane, and NH_4Cl (99.998%) were purchased from Aldrich, and 2,2,6,6-tetramethyl-3,5-heptanedione was purchased from Lancaster Synthesis or Oakwood Chemicals. High-purity (99.999%) Ln_2O_3 (Ln = Ce, Nd, Gd, Er) was obtained from Cerac. Gelest supplied $KN(SiMe_3)_2$ (11% solution in toluene). $Ce(dpm)_4$ and $Er(dpm)_3$ were purchased from Strem and were handled and stored under N_2. All reagents were used as received.

Physical Measurements. ^1H NMR spectra were recorded in $CDCl_3$ or dry, deoxygenated C_6D_6 on either a Varian Gemini 300 MHz, Varian Mercury 400 MHz, or Varian Unity 500 MHz spectrometer. Chemical shifts were referenced to solvent signals. Elemental analyses were performed by Midwest Microlabs, Inc. (Indianapolis, IN). Melting points were determined in sealed

(75) Edleman, N. L.; Belot, J. A.; Babcock, J. R.; Metz, A. W.; Metz, M. V.; Stern, C. L.; Marks, T. J. *Mater. Res. Soc. Symp. Proc.* **2000**, *623*, 371−376.
(76) Wang, A.; Belot, J. A.; Marks, T. J.; Markworth, P. R.; Chang, R. P. H.; Chudzik, M. P.; Kannewurf, C. R. *Physica C* **1999**, *320*, 154−160.
(77) Belot, J. A.; Wang, A.; McNeely, R. J.; Liable-Sands, L.; Rheingold, A. L.; Marks, T. J. *Chem. Vap. Deposition* **1999**, *5*, 65−69.
(78) Belot, J. A.; Wang, A.; Edleman, N. L.; Babcock, J. R.; Metz, M. V.; Marks, T. J.; Markworth, P. R.; Chang, R. P. H. *Mater. Res. Soc. Symp. Proc.* **1999**, *574*, 37−43.
(79) Studebaker, D. B.; Neumayer, D. A.; Hinds, B. J.; Stern, C. L.; Marks, T. J. *Inorg. Chem.* **2000**, *39*, 3148−3157.
(80) Neumayer, D. A.; Belot, J. A.; Feezel, R. L.; Reedy, C. J.; Stern, C. L.; Marks, T. J.; Liable-Sands, L. M.; Rheingold, A. L. *Inorg. Chem.* **1998**, *37*, 5625−5633.
(81) Schulz, D. L.; Hinds, B. J.; Neumayer, D. A.; Stern, C. L.; Marks, T. J. *Chem. Mater.* **1993**, *5*, 1605−1617.
(82) Schulz, D. L.; Hinds, B. J.; Stern, C. L.; Marks, T. J. *Inorg. Chem.* **1993**, *32*, 249−250.
(83) Galasso, F. S. *Structure and Properties of Inorganic Solids*; International Series of Monographs in Solid State Physics; Pergamon: New York, 1970; Vol. 7, p 93.
(84) Inoue, T.; Yamamoto, Y.; Koyama, S.; Suzuki, S.; Ueda, Y. *Appl. Phys. Lett.* **1990**, *29*, 1332−1333.
(85) Yoshimoto, M.; Shimozono, K.; Maeda, T.; Ohnishi, T.; Kumagai, M.; Chikyow, T.; Ishiyama, O.; Shinohara, M.; Koinuma, H. *Jpn. J. Appl. Phys.* **1995**, *34*, L688−L690.
(86) Denhoff, M. W.; McCaffrey, J. P. *J. Appl. Phys.* **1991**, *70*, 3986−3988.
(87) Wu, X. D.; Dye, R. C.; Muenchansen, R. E.; Foltyn, S. R.; Maley, M.; Rollett, A. D.; Garcia, A. R.; Nogar, N. S. *Appl. Phys. Lett.* **1991**, *58*, 2165−2167.
(88) Yaegashi, S.; Kurihara, T.; Hoshi, H.; Segawa, H. *Jpn. J. Appl. Phys.* **1994**, *33*, 270−274.
(89) Guo, S.; Arwin, H.; Jacobson, S. N.; Jarrendahl, K.; Helmersson, U. *J. Appl. Phys.* **1995**, *77*, 5369−5376.
(90) Wang, F.; Kunkel, G.; Coppetti, C.; Kohlstedt, H.; Wordenweber, R. *Appl. Supercond.* **1993**, *2*, 155−1158.
(91) Inoue, T.; Ohsuna, T.; Luo, L.; Wu, X. D.; Maggiore, C. J.; Yamamoto, Y.; Koyama, S.; Chang, H. *Appl. Phys. Lett.* **1991**, *59*, 3604−3606.
(92) Kotelyanskii, I. M.; Luzanov, V. A.; Yu, M.; Dikaev, M.; Kravchenko, V. B.; Melekh, B. J. *Thin Solid Films* **1996**, *280*, 163−166.
(93) Becht, M.; Morishita, T. *Chem. Vap. Deposition* **1996**, *2*, 191−197.
(94) Merchant, P.; Jacowitz, R. D.; Tibbs, K.; Taber, R. C.; Laderman, S. S. *Appl. Phys. Lett.* **1992**, *60*, 763−765.

capillary tubes with an uncalibrated MelTemp melting point apparatus. Thermogravimetric analysis data were collected under 5.0 (± 0.1) Torr of N_2 with a TA Instruments SDT 2960 simultaneous DTA−TGA instrument. Weight loss data and subsequent activation data were collected at a ramp rate of 1.5 °C/min, while isothermal data were recorded at 155 °C.

Synthesis of β-Ketoimine Ligands [H($R_1R_2R_3$)]. The β-diketones 2,2-dimethyl-3,5-hexanedione and 2,2-dimethyl-3,5-heptanedione were synthesized according to a literature procedure.[95] β-Ketoimines based on 2,2,6,6-tetramethyl-3,5-heptanedione (Hdpm) were prepared by neat reaction of the trimethylsilyl enol ether derivative of Hdpm with the amino ether following general literature procedure.[96] All other β-ketoimine ligands were synthesized by condensation of the appropriate β-diketone with the corresponding amino ethers in benzene.[97] The pure β-ketoimine ligands were dried over $MgSO_4$ or molecular sieves overnight and then distilled in vacuo directly onto molecular sieves in a nitrogen-filled storage tube to ensure anhydrous quality.

Synthesis of 2,2-Dimethyl-5-*N*-(2-methoxyethyl-imino)-3-hexanone, [H(ᵗBuMeMe)] (1). In a 250 mL round bottom flask fitted with reflux condenser and Dean−Stark trap, 27.4 g (194 mmol) of 2,2-dimethyl-3,5-hexanedione was dissolved in 100 mL of benzene. While the reaction mixture was stirred rapidly, 16.0 g (214 mmol) of 2-methoxyethylamine was added and the reaction mixture refluxed overnight. Water was collected in the Dean−Stark trap as the reaction progressed. Residual water was removed azeotropically, followed by distillation of benzene. The resulting yellow liquid was then distilled in vacuo at 115 °C/300 mTorr to afford 28.7 g of compound **1** as a pale yellow liquid (74.3% yield). ^{1}H NMR (300 MHz, $CDCl_3$, δ): 1.15 [s, 9 H, C(C*H*$_3$)$_3$], 1.99 [s, 3 H, C(NH)-C*H*$_3$], 3.36 [s, 3 H, OC*H*$_3$], 3.42 [m, 2 H, NHCH$_2$C*H*$_2$OCH$_3$], 3.53 [m, 2 H, NHC*H*$_2$CH$_2$OCH$_3$], 5.12 [s, 1 H, C(O)C*H*C(NH)], 10.99 [br s, 1 H, N*H*]. Anal. Calcd for $C_{11}H_{21}O_2N$: C, 66.29; H, 10.62; N, 7.03. Found: C, 66.46; H, 10.73; N, 7.13.

Synthesis of 2,2-Dimethyl-5-*N*-(2-methoxyethyl-imino)-3-heptanone, [H(ᵗBuEtMe)] (2). This compound was prepared analogously to compound **1**, starting with 30.0 g (192 mmol) of 2,2-dimethyl-3,5-heptanedione and 15.8 g (211 mmol) of 2-methoxyethylamine. The resulting yellow liquid was distilled at 82 °C/200 mTorr to afford 28.7 g of compound **2** as a pale yellow liquid (78.7% yield). ^{1}H NMR (300 MHz, $CDCl_3$, δ): 1.15 [s, 9 H, C(C*H*$_3$)$_3$], 1.16 [t, 3 H, CH$_2$C*H*$_3$], 2.28 [q, 2 H, C*H*$_2$CH$_3$], 3.39 [s, 3 H, OC*H*$_3$], 3.43 [m, 2 H, NHCH$_2$C*H*$_2$OCH$_3$], 3.54 [m, 2 H, NHC*H*$_2$CH$_2$OCH$_3$], 5.18 [s, 1 H, C(O)C*H*C(NH)], 11.02 [br s, 1 H, N*H*]. Anal. Calcd for $C_{12}H_{23}O_2N$: C, 67.57; H, 10.87; N, 6.57. Found: C, 68.39; H, 10.94; N, 5.97.

Synthesis of 2,2,6,6-Tetramethyl-5-*N*-(2-methoxyethyl-imino)-3-heptanone, [H(ᵗBuᵗBuMe)] (3). In a 250 mL round bottom flask fitted with reflux condenser was placed at 26 g (102 mmol) of 4-ene-2,2,6,6-tetramethylsiloxy-3-heptanedione. While the reaction mixture was stirred rapidly, 8.4 g (112 mmol) of 2-methoxyethylamine was added and the reaction mixture heated to 90−95 °C overnight. The resulting yellow liquid was distilled twice in vacuo at 87 °C/500 mTorr to afford 9.1 g of compound **3** as a pale yellow liquid (37.0% yield). ^{1}H NMR (300 MHz, $CDCl_3$, δ): 1.15 [s, 9 H, C(O)C(C*H*$_3$)$_3$], 1.26 [s, 9 H, C(NH)C(C*H*$_3$)$_3$], 3.41 [s, 3 H, OC*H*$_3$], 3.59 [m, 2 H, NHCH$_2$C*H*$_2$OCH$_3$], 3.65 [m, 2 H, NHC*H*$_2$-CH$_2$OCH$_3$], 5.33 [s, 1 H, C(O)C*H*C(NH)], 11.62 [br s, 1 H, N*H*]. Anal. Calcd for $C_{14}H_{27}O_2N$: C, 69.67; H, 11.27; N, 5.80. Found: C, 69.54; H, 11.35; N, 5.95.

Synthesis of Anhydrous Lanthanide Chlorides, $LnCl_3$, Ln^{3+} = Ce^{3+}, Nd^{3+}, Gd^{3+}, Er^{3+}. Anhydrous $LnCl_3$ reagents were obtained in near-quantitative yield by reaction of the corresponding Ln_2O_3 with excess NH_4Cl (>10 equiv for Ln = La−Gd; >12 equiv for Ln = Tb−Lu, Y, Sc) via modification of a published procedure.[98] Commercial oxides and NH_4Cl were placed in a large beaker and dissolved in 4:3 H_2O:concentrated HCl. The resulting solution (0.3 M in Ln) was slowly evaporated to dryness with careful stirring. The solid obtained was then ground in a mortar and pestle and placed in a Schlenk sublimation tube, which was then placed in a tube furnace and heated according to the following schedule in vacuo (~1 Torr): 1 day, 140 °C (to drive off excess water); 1 day, 250 °C [to form $(NH_4)_2LnCl_5$ for Ln = La−Gd or $(NH_4)_3LnCl_6$ for La = Tb−Lu, Y, Sc]; 1 day, 360 °C (to decompose the complex chlorides and drive off any excess NH_4Cl). The tube was then allowed to cool and taken directly into the glovebox, where the solid $LnCl_3$ was collected and stored.

Synthesis of Lanthanide Tris[bis(trimethylsilyl)amides], Ln[N(SiMe$_3$)$_2$]$_3$, Ln^{3+} = Ce^{3+}, Nd^{3+}, Gd^{3+}, Er^{3+}. The lanthanide amides were synthesized following a modified literature procedure.[99] $KN(SiMe_3)_2$ was reacted in a mixture of 1:1 THF:toluene with excess anhydrous $LnCl_3$ to afford the corresponding $Ln[N(SiMe_3)_2]_3$ complex. The crude solid was then purified by repeated fractional vacuum sublimation. Final recrystallization from pentane (−78 °C) after sublimation led to purer $Ln[N(SiMe_3)_2]_3$ reagents. Impurities [unreacted alkali metal amide and/or $HN(SiMe_3)_2$] were typically present at 3−5 mol % in the final product as judged by NMR. $SiMe_3$ ^{1}H NMR shifts found for these amides are as follows (500 MHz, C_6D_6, δ): $Ce[N(SiMe_3)_2]_3$, −3.39; $Nd[N(SiMe_3)_2]_3$, −6.25; $Gd[N(SiMe_3)_2]_3$, −11.07; $Er[N(SiMe_3)_2]_3$, 62.89.

Synthesis of Lanthanide Tris-β-ketoiminates, Ln($R_1R_2R_3$)$_3$, Ln^{3+} = Ce^{3+}, Nd^{3+}, Gd^{3+}, Er^{3+}. Tris[2,2-dimethyl-5-*N*-(2-methoxyethyl-imino)-3-hexanato]cerium(III), [Ce(ᵗBuMeMe)$_3$] (4). In the glovebox, a two-neck, 100 mL round bottom flask fitted with a rubber septum, magnetic stir bar, and reflux condenser with vacuum adapter was charged with 1.49 g of $Ce[N(SiMe_3)_2]_3$ (2.40 mmol). The reaction vessel was then removed from the glovebox and immediately interfaced to a Schlenk line, and 24 mL of xylenes was added via syringe. The reaction flask was then immersed in a preheated oil bath (~150 °C) and the reaction mixture stirred until homogeneous. Immediately, 1.57 g of ligand **1** (7.90 mmol) was injected into the reaction flask, and the solution was refluxed overnight (14 h), gradually changing color from golden yellow to a deeper amber. The volatiles were then removed in vacuo (1 Torr), and the resulting waxy amber solid was recrystallized from pentane at −30 °C to afford 1.50 g of amber crystalline **4** (85% yield); mp 95−98 °C. ^{1}H NMR (300 MHz, C_6D_6, δ): −10.8, −8.4, −2.4, 1.2, 1.6, 2.6, 2.8, 5.1, 13.5. Anal. Calcd for $C_{33}H_{60}O_6N_3Ce$: C, 53.93; H, 8.23; N, 5.72. Found: C, 53.60; H, 8.26; N, 5.44.

Tris[2,2-dimethyl-5-*N*-(2-methoxyethyl-imino)-3-hexanato]-neodymium(III), [Nd(ᵗBuMeMe)$_3$] (5). This Nd complex was prepared analogously to compound **4**, starting with 1.50 g of Nd[N(SiMe$_3$)$_2$]$_3$ (2.40 mmol) and 1.57 g of ligand **1** (7.90 mmol). The reaction mixture changed color from bright blue to a blue-green. The resulting waxy blue-green solid was recrystallized from pentane at −30 °C to afford 1.51 g of blue-green crystalline **5** (85% yield);

(95) Swamer, F. W.; Hauser, C. R. *J. Am. Chem. Soc.* **1950**, *72*, 1352−1356.
(96) Shin, H.-K.; Hampden-Smith, M. J.; Kodas, T. T.; Rheingold, A. L. *J. Chem. Soc., Chem. Commun.* **1992**, 217−219.
(97) Moffett, R. B.; Hoehn, W. M. *J. Am. Chem. Soc.* **1947**, *69*, 1792−1794.
(98) Meyer, G.; Garcia, E.; Corbett, J. D. *Inorg. Synth.* **1989**, *25*, 146−150.
(99) Bradley, D. C.; Ghotra, J. S.; Hart, F. A. *J. Chem. Soc., Dalton Trans.* **1973**, 1021−1023.

mp 78−81 °C. ^{1}H NMR (300 MHz, C_6D_6, δ): −18.8, −14.6, −3.2, −0.3, 1.2, 1.6, 3.0, 7.9, 16.2. Anal. Calcd for $C_{33}H_{60}O_6N_3Nd$: C, 53.63; H, 8.18; N, 5.69. Found: C, 53.84; H, 8.10; N, 5.62.

Tris[2,2-dimethyl-5-*N*-(2-methoxyethyl-imino)-3-hexanato]-gadolinium(III), [Gd(^{t}BuMeMe)$_3$] (6). This Gd complex was prepared analogously to compound **4**, starting with 1.60 g of Gd[N(SiMe$_3$)$_2$]$_3$ (2.50 mmol) and 1.65 g of ligand **1** (8.30 mmol). The reaction mixture changed color from colorless to a light orange. The resulting waxy orange solid was recrystallized from pentane at −30 °C to afford 0.95 g of light orange crystalline **6** (51% yield); mp 76−78 °C. ^{1}H NMR studies were not possible due to the highly paramagnetic nature ($4f^7$) of this complex. Anal. Calcd for $C_{33}H_{60}O_6N_3Gd$: C, 52.70; H, 8.04; N, 5.59. Found: C, 52.70; H, 8.05; N, 5.44.

Tris[2,2-dimethyl-5-*N*-(2-methoxyethyl-imino)-3-hexanato]erbium(III), [Er(^{t}BuMeMe)$_3$] (7). This Er complex was prepared analogously to compound **4**, starting with 1.56 g of Er[N(SiMe$_3$)$_2$]$_3$ (2.40 mmol) and 1.57 g of ligand **1** (7.90 mmol). The reaction mixture changed color from pink to orange. The resulting waxy orange solid was recrystallized from pentane at −30 °C to afford 1.55 g of bright orange crystalline **7** (85% yield); mp 65−68 °C. ^{1}H NMR (300 MHz, C_6D_6, δ): −47.9, −15.8, −2.5, 0.8, 1.6, 1.8, 2.6, 5.2, 35.5. Anal. Calcd for $C_{33}H_{60}O_6N_3Er$: C, 52.01; H, 7.94; N, 5.51. Found: C, 51.89; H, 8.21; N, 5.61.

Tris[2,2-dimethyl-5-*N*-(2-methoxyethyl-imino)-3-heptanato]-cerium(III), Ce(^{t}BuEtMe)$_3$] (8). This Ce complex was prepared analogously to compound **4**, starting with 1.49 g of Ce[N(SiMe$_3$)$_2$]$_3$ (2.40 mmol) and 1.68 g of ligand **2** (7.90 mmol). The reaction mixture changed color from golden yellow to a deeper amber. The resulting waxy amber solid was recrystallized from pentane at −30 °C to afford 0.89 g of amber crystalline **8** (49% yield); mp 99−101 °C. ^{1}H NMR (500 MHz, C_6D_6, δ): −10.3, −8.2, −2.0, 1.2, 2.1, 5.1, 12.9. Anal. Calcd for $C_{36}H_{66}O_6N_3Ce$: C, 55.65; H, 8.56; N, 5.41. Found: C, 55.57; H, 8.74; N, 5.52.

Tris[2,2-dimethyl-5-*N*-(2-methoxyethyl-imino)-3-heptanato]-neodymium(III), [Nd(^{t}BuEtMe)$_3$] (9). This Nd complex was prepared analogously to compound **4**, starting with 0.81 g of Nd[N(SiMe$_3$)$_2$]$_3$ (1.30 mmol) and 0.92 g of ligand **2** (4.30 mmol). The reaction mixture changed color from bright blue to a blue-green. The resulting waxy blue-green solid was recrystallized from pentane at −30 °C to afford 0.63 g of blue-green crystalline **9** (62% yield); mp 85−88 °C. ^{1}H NMR (400 MHz, C_6D_6, δ): −19.3, −15.1, −2.9, 0.7, 7.9, 16.0. Anal. Calcd for $C_{36}H_{66}O_6N_3Nd$: C, 55.35; H, 8.52; N, 5.38; Found: C, 55.43; H, 8.45; N, 5.47.

Tris[2,2-dimethyl-5-*N*-(2-methoxyethyl-imino)-3-heptanato]-erbium(III), [Er(^{t}BuEtMe)$_3$] (10). This Er complex was prepared analogously to compound **4**, starting with 1.57 g of Er[N(SiMe$_3$)$_2$]$_3$ (2.40 mmol) and 1.70 g of ligand **2** (7.90 mmol). The reaction mixture changed color from pink to orange. The resulting waxy orange solid was recrystallized from pentane at −30 °C to afford 0.84 g of bright orange crystalline **10** (44% yield); mp 81−82 °C. ^{1}H NMR (500 MHz, C_6D_6, δ): −81.0, −49.4, −16.7, −2.7, 1.8, 35.6. Anal. Calcd for $C_{36}H_{66}O_6N_3Er$: C, 53.77; H, 8.27; N, 5.23; Found: C, 53.52; H, 8.46; N, 5.27.

Tris[2,2,6,6-tetramethyl-5-*N*-(2-methoxyethyl-imino)-3-heptanato]neodymium(III), [Nd(^{t}Bu^{t}BuMe)$_3$] (11). This Nd complex was prepared analogously to compound **4**, starting with 1.10 g of Nd[N(SiMe$_3$)$_2$]$_3$ (1.80 mmol) and 1.40 g of ligand **3** (5.80 mmol). The reaction mixture changed color from bright blue to a blue-green. The resulting waxy blue-green solid was recrystallized from pentane at −30 °C to afford 0.74 g of blue-green crystalline **11** (49% yield); mp 125−127 °C. ^{1}H NMR (400 MHz, C_6D_6, δ): −31.4, −19.6, −1.3, 8.7, 15.5, 21.8. Anal. Calcd for $C_{42}H_{78}O_6N_3Nd$: C, 58.30; H, 9.09; N, 4.86. Found: C, 58.48; H, 9.14; N, 4.60.

Tris[2,2,6,6-tetramethyl-5-*N*-(2-methoxyethyl-imino)-3-heptanato]erbium(III), [Er(^{t}Bu^{t}BuMe)$_3$] (12). This Er complex was prepared analogously to compound **4**, starting with 1.00 g of Er[N(SiMe$_3$)$_2$]$_3$ (1.50 mmol) and 1.23 g of ligand **3** (5.10 mmol). The reaction mixture changed color from pink to orange. The resulting waxy orange solid was recrystallized from pentane at −30 °C to afford 0.93 g of bright orange crystalline **12** (70% yield); mp 135−143 °C. ^{1}H NMR (400 MHz, C_6D_6, δ): −8.0, −5.5. Anal. Calcd for $C_{42}H_{78}O_6N_3Er$: C, 56.79; H, 8.85; N, 4.73; Found: C, 56.25; H, 8.71; N, 4.29.

Single-Crystal X-ray Diffraction Studies. X-ray data for single crystals of lanthanide complexes **4**−**7**, **9**, **10**, and **12** [grown from pentane solution and mounted on a glass fiber with Paratone-N (Exxon)] were collected on a CCD area detector with graphite-monochromated Mo Kα radiation. Reflections were collected with a Bruker SMART detector and processed with SAINT-NT from Bruker. Data were corrected for Lorentz and polarization effects. The structures were solved by direct methods and expanded using Fourier techniques. The non-hydrogen atoms were refined anisotropically. Hydrogen atoms were included but not refined. All calculations were performed using the Bruker SHELXTL crystallographic software package. The space groups for **4**, **5**, **6**, **7**, **9**, **10**, and **12** were determined to be $P\bar{1}$, $P2_1/c$, $P2_1/n$, $P\bar{1}$, $P\bar{1}$, $P2_1/c$, and $P2_1/c$, respectively, based on a statistical analysis of intensity distributions, and the successful solution and refinement of the structures. Important experimental parameters for these structure determinations are tabulated in Tables 1−3. The asymmetric unit of complex **4** contains four crystallographically independent, but chemically equivalent, molecules. Also, the two *tert*-butyl groups at C(21) and C(44) and the methoxy group at C(50) in compound **5** are disordered over two equally occupied positions. The effect on the metrical parameters of interest is negligible. Data for all these complexes has been deposited at the Cambridge Crystallographic Database Center.[100]

Film Growth Experiments. MOCVD of CeO_2 thin films was carried out in the low-pressure, horizontal, cold-wall MOCVD system described elsewhere.[26] The metal−organic precursor and the reactant gas (100 sccm of O_2; sccm = standard cubic centimeters per minute) vapor streams were mixed immediately upstream of the reactor. The precursor was maintained at 150−160 °C and introduced into the reactor using ultrahigh-purity Ar flowing at 70 sccm. Deposition was carried out at a system pressure of 3.5 Torr, and the single-crystal (001) YSZ substrates (purchased from Materials Technology International, Inc.) were externally heated by an IR heater to 450−650 °C. To verify the viability of low-temperature CeO_2 MOCVD deposition for HTS buffers, pulsed organometallic beam epitaxy (POMBE) was employed to deposit YBCO films at 725 °C on the MOCVD-derived CeO_2/YSZ (001) structures. Details of the YBCO deposition process have been described elsewhere.[101] Growth parameter dependence of deposited film structure, crystallinity, and thickness were investigated by Ni-filtered Cu Kα $\theta-2\theta$ and ϕ scan X-ray diffraction (XRD; Matrix and Scintag XDS 2000 instruments) and cross-sectional transmission

(100) Supplementary crystallographic data for complexes **4** (114935), **5** (174766), **6** (175017), **7** (174765), **9** (178184), **10** (178185), and **12** (178272) can be obtained free of charge from the Cambridge Crystallographic Database Center (CCDC) via www.ccdc.cam.ac.uk/conts/retrieving.html (or from the CCDC, 12 Union Road, Cambridge CB2 1EZ, U.K.; fax, +44 1223 336033; e-mail, deposit@ccdc.cam.ac.uk).

(101) Duray, S. J.; Buchholz, D. B.; Song, S. N.; Richeson, D. S.; Ketterson, J. B.; Marks, T. J.; Chang, R. P. H. *Appl. Phys. Lett.* **1991**, *59*, 1503−1505.

Table 1. Crystal Data and Structure Refinement for Compounds **4**, **5**, and **6**

complex identity	Ce(ᵗBuMeMe)₃, **4**	Nd(ᵗBuMeMe)₃, **5**	Gd(ᵗBuMeMe)₃, **6**
empirical formula	$C_{33}H_{60}N_3O_6Ce$	$C_{33}H_{60}N_3O_6Nd$	$C_{33}H_{60}N_3O_6Gd$
fw	734.96	739.08	752.09
temp (K)	198(2)	198(2)	153(2)
wavelength (Å)	0.71073	0.71073	0.71073
cryst syst, space group	triclinic, $P\bar{1}$	monoclinic, $P2_1/c$	monoclinic, $P2_1/c$
unit cell dimens (Å)			
a	17.5040(2)	13.3606(2)	10.6115(6)
b	21.1598(2)	17.1475(2)	25.2146(15)
c	23.0715(2)	16.4002(2)	14.1149(9)
unit cell angles (deg)			
α	112.8853(6)	90.00	90.00
β	90.9699(11)	98.9027(7)	100.8080(10)
γ	99.5012(7)	90.00	90.00
vol (Å³)	7733.63(12)	3712.02(8)	3709.7(4)
Z, calcd density (g/cm³)	8, 1.262	4, 1.322	4, 1.347
abs coeff (mm^{-1})	1.218	1.441	1.830
F(000)	3080	1548	1564
cryst size (mm)	0.20 × 0.20 × 0.10	0.30 × 0.20 × 0.15	0.31 × 0.20 × 0.16
θ range for data collection (deg)	0.96−28.13	1.73−26.00	1.62−28.95
limiting indices	$-22 \le h \le 23$ $-28 \le k \le 27$ $-29 \le l \le 23$	$-17 \le h \le 15$ $0 \le k \le 19$ $0 \le l \le 21$	$-14 \le h \le 14$ $-32 \le k \le 33$ $-19 \le l \le 18$
reflns collected/ unique	49148/32224 [*R*(int) = 0.0407]	8579/4865 [*R*(int) = 0.1134]	33706/9106 [*R*(int) = 0.0278]
completeness to *θ* = 28.13° (%)	85.1	98.7	92.6
abs correction	none	DIFABS	none
refinement meth	full-matrix least-squares on F^2		
data/restraints/ params	32224/0/1549	4735/0/402	9106/0/388
GOF on F^2	1.120	1.667	1.058
final *R* indices [$I > 2\sigma(I)$][a]	R1 = 0.0528 wR2 = 0.1157	R1 = 0.0851 wR2 = 0.2306	R1 = 0.0324 wR2 = 0.0780
R indices (all data)[a]	R1 = 0.0884 wR2 = 0.1326	R1 = 0.1159 wR2 = 0.2713	R1 = 0.0403 wR2 = 0.0816
largest diff peak and hole ($e^-/Å^{-3}$)	0.987 and −2.307	0.822 and −1.100	2.462 and −0.710

[a] $R1 = \sum||F_o| - |F_c||/\sum|F_o|$ and $wR2 = \{\sum[w(F_o^2 - F_c^2)^2]/\sum[w(F_o^2)^2]\}^{1/2}$, where $w = 1/[\sigma^2(F_o^2) + (0.1551P)^2 + 0.0000P]$ and $P = (F_o^2 + 2F_c^2)/3$.

Table 2. Crystal Data and Structure Refinement for Compounds **7**, **9**, and **10**

complex identity	Er(ᵗBuMeMe)₃, **7**	Nd(ᵗBuEtMe)₃, **9**	Er(ᵗBuEtMe)₃, **10**
empirical formula	$C_{33}H_{60}N_3O_6Er$	$C_{36}H_{66}N_3O_6Nd$	$C_{36}H_{66}N_3O_6Er$
fw	762.10	781.16	804.18
temp (K)	293(2)	153(2)	153(2)
wavelength (Å)	0.71073	0.71073	0.71073
cryst syst, space group	triclinic, $P\bar{1}$	triclinic, $P\bar{1}$	monoclinic, $P2_1/c$
unit cell dimens (Å)			
a	10.0926(1)	11.5887(9)	21.0002(12)
b	11.0198(1)	12.5994(9)	9.8643(6)
c	18.5054(1)	14.6711(11)	19.3381(11)
unit cell angles (deg)			
α	102.882(1)	97.6820(10)	90
β	97.346(2)	97.7390(10)	91.3530(10)
γ	108.370(1)	104.2170(10)	90
vol (Å³)	1859.92(2)	2026.4(3)	4004.8(4)
Z, calcd density (g/cm³)	2, 1.361	2, 1.280	4, 1.334
abs coeff (mm^{-1})	1.218	1.323	2.138
F(000)	790	822	1676
cryst size (mm)	0.40 × 0.30 × 0.15	0.36 × 0.16 × 0.18	0.228 × 0.180 × 0.070
θ range for data collection (deg)	2.03−24.00	1.42−28.30	0.97−28.34
limiting indices	$-11 \le h \le 10$ $-12 \le k \le 11$ $-21 \le l \le 20$	$-15 \le h \le 15$ $-16 \le k \le 16$ $-19 \le l \le 19$	$-27 \le h \le 26$ $-13 \le k \le 12$ $-24 \le l \le 25$
reflns collected/ unique	10894/5714 [*R*(int) = 0.0357]	18669/9373 [*R*(int) = 0.0217]	35724/9618 [*R*(int) = 0.0312]
completeness to *θ* = 28.13° (%)	97.8	92.9	96.3
abs correction	none	face centered and SADABS	
refinement meth	full-matrix least-squares on F^2		
data/restraints/ params	5714/0/389	9373/0/415	9618/0/415
GOF on F^2	1.149	1.062	1.049
final *R* indices [$I > 2\sigma(I)$][a]	R1 = 0.0318 wR2 = 0.0957	R1 = 0.0299 wR2 = 0.0736	R1 = 0.0269 wR2 = 0.0649
R indices (all data)[a]	R1 = 0.0360 wR2 = 0.1026	R1 = 0.0356 wR2 = 0.0764	R1 = 0.0358 wR2 = 0.0683
largest diff peak and hole ($e^-/Å^{-3}$)	1.869 and −0.754	1.324 and −0.701	2.342 and −0.605

[a] $R1 = \sum||F_o| - |F_c||/\sum|F_o|$ and $wR2 = \{\sum[w(F_o^2 - F_c^2)^2]/\sum[w(F_o^2)^2]\}^{1/2}$, where $w = 1/[\sigma^2(F_o^2) + (0.1551P)^2 + 0.0000P]$ and $P = (F_o^2 + 2F_c^2)/3$.

electron microscopy (TEM; Hitachi S4500 FE instrument). Conventional four-probe methods were used for measuring the YBCO film critical current density, J_c, and the YBCO superconducting transition temperature, T_c, was measured inductively. Electrical characterization techniques have been outlined elseware.[26] Film surface roughness and morphology were analyzed with a Digital Instruments Nanoscope IIIa atomic force microscope (AFM) used in the contact mode.

Results

The synthesis of monomeric lanthanide complexes of type **VIII** is outlined here. These compounds are low-melting, thermally stable, and volatile, despite the fact that they contain no fluorinated substituents. Studies of alkyl substitution at the ligand keto, imino, and ether sites and the resulting lanthanide complex melting point and volatility variation are also detailed. Implementation of a new type **VIII** precursor in heteroepitaxial CeO_2 thin film growth for superconductor current-carrying applications is also described.

MOCVD Precursor Synthesis. The present lanthanide *β*-ketoiminate complexes are synthesized in a single-step amine elimination reaction by refluxing the corresponding lanthanide tris[bis(trimethylsilyl)amide] with excess free ligand (see Figure 1 for the nomenclature scheme) in high-boiling xylenes overnight (eq 1). In this procedure, the

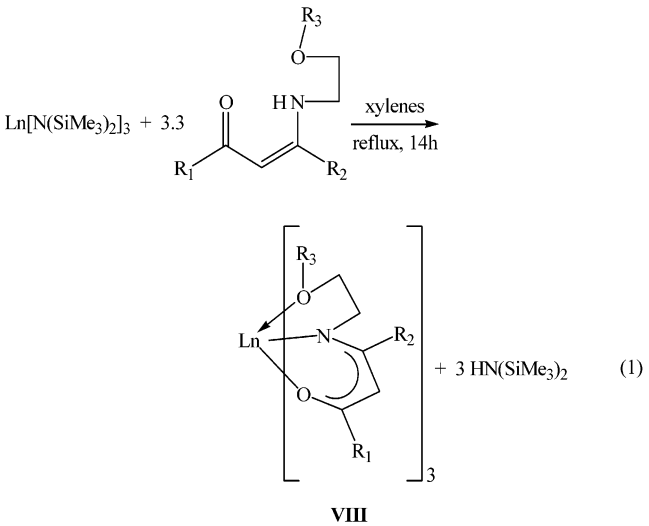

(1)

VIII

desired species are readily isolated, since the only reaction byproduct is volatile $HN(SiMe_3)_2$. The products are purified

Table 3. Crystal Data and Structure Refinement for Compound **12**

complex identity	$Er(^tBu^tBuMe)_3$, **12**
empirical formula	$C_{42}H_{78}N_3O_6Er$
fw	888.33
temp (K)	153(2)
wavelength (Å)	0.71073
cryst syst, space group	monoclinic, $P2_1/c$
unit cell dimens (Å)	
a	10.3100(7)
b	27.3356(17)
c	17.4357(11)
unit cell angles (deg)	
α	90
β	105.4000(10)
γ	90
vol (Å^3)	4737.5(5)
Z, calcd density (g/cm^3)	4, 1.245
abs coeff (mm^{-1})	1.814
F(000)	1868
cryst size (mm)	0.36 × 0.39 × 0.30
θ range for data collection (deg)	1.42−28.30
limiting indices	$-13 \le h \le 13$ $-36 \le k \le 35$ $-17 \le l \le 22$
reflns collected/unique	34982/11218 [*R*(int) = 0.0190]
completeness to $\theta = 28.30°$ (%)	95.3
abs correction	face and SADABS
refinement meth	full-matrix least-squares on F^2
data/restraints/params	11218/0/469
GOF on F^2	1.038
final *R* indices [$I > 2\sigma(I)$][a]	R1 = 0.0250, wR2 = 0.0597
R indices (all data)[a]	R1 = 0.0295, wR2 = 0.0621
largest diff peak and hole (e$^-$/Å^{-3})	1.812 and −0.696

[a] $R1 = \sum||F_o| - |F_c||/\sum|F_o|$ and $wR2 = \{\sum[w(F_o^2 - F_c^2)^2]/\sum[w(F_o^2)^2]\}^{1/2}$, where $w = 1/[\sigma^2(F_o^2) + (0.1551P)^2 + 0.0000P]$ and $P = (F_o^2 + 2F_c^2)/3$.

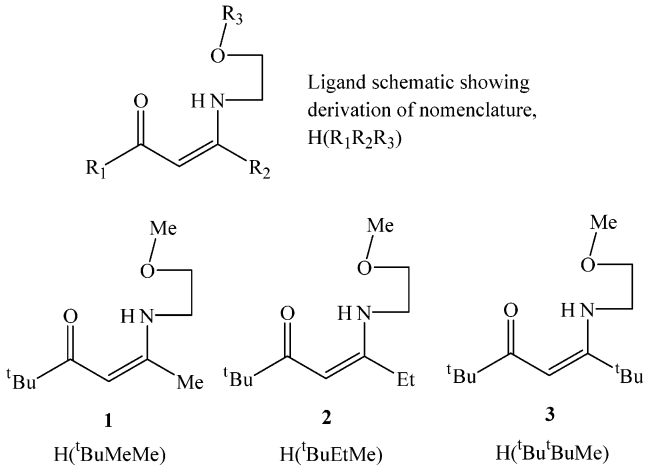

Figure 1. Schematic representation of the *β*-ketoimine ligands synthesized in this study.

by recrystallization from pentane to yield homoleptic, monomeric, colorful lanthanide complexes (Ce^{3+}, amber; Nd^{3+}, blue-green; Gd^{3+}, light orange; Er^{3+}, bright orange; see Figure 2 for a schematic representation of the complexes isolated). Synthetic yields are listed in Table 4. The complexes are stable under an inert atmosphere and can be readily and easily sublimed at 80−110 °C/10^{-4} Torr. Melting points are in the 60−130 °C range (Table 4), affording liquid, constant surface area, thermally stable precursors at operating MOCVD precursor reservoir temperatures.

Precursor Melting Point Trends. Alkyl ligand substituents were deliberately selected such that lanthanide precursor physical properties could be assessed with respect to

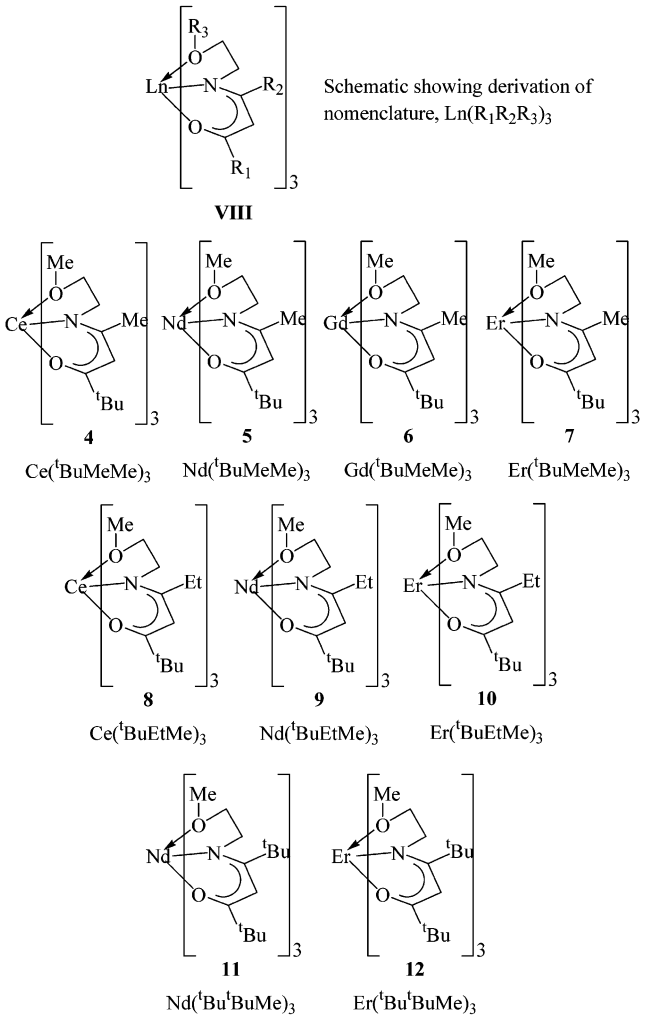

Figure 2. Idealized representation of the lanthanide *β*-ketoiminato complexes synthesized in this study. Note that not all ether oxygen atoms are coordinated in all complexes.

Table 4. Synthetic Yield, Melting Point, and Coordination Number of New *β*-Ketoiminate Lanthanide MOCVD Precursors

complex name	synthetic yield (%)	mp (°C)	coord no.[a]
4, $Ce(^tBuMeMe)_3$	85	95−98	8
5, $Nd(^tBuMeMe)_3$	85	78−81	8
6, $Gd(^tBuMeMe)_3$	51	76−78	8
7, $Er(^tBuMeMe)_3$	85	65−68	7
8, $Ce(^tBuEtMe)_3$	49	99−101	8[b]
9, $Nd(^tBuEtMe)_3$	62	85−88	8
10, $Er(^tBuEtMe)_3$	44	81−82	7
11, $Nd(^tBu^tBuMe)_3$	49	125−128	8[b]
12, $Er(^tBu^tBuMe)_3$	70	135−143	7

[a] As determined from single-crystal X-ray diffraction. [b] Assumed.

substitution effects at a particular molecular site. As summarized in Table 4 and shown in Figure 3, two melting point trends are noteworthy. First, the melting point decreases with ionic radius across the lanthanide series for a given ligand system (i.e., mp **4**, 95−98 °C; **5**, 78−81 °C; **6**, 76−78 °C; **7**, 65−68 °C; see Figure 3a). Second, introduction of larger alkyl groups (e.g., substitution of ethyl or *tert*-butyl for methyl) at the R_2 site results in an increase in melting point (i.e., mp **5**, 78−81 °C; **9**, 85−88 °C; **11**, 125−128 °C; see Figure 3b). Attempts to synthesize complexes with substit-

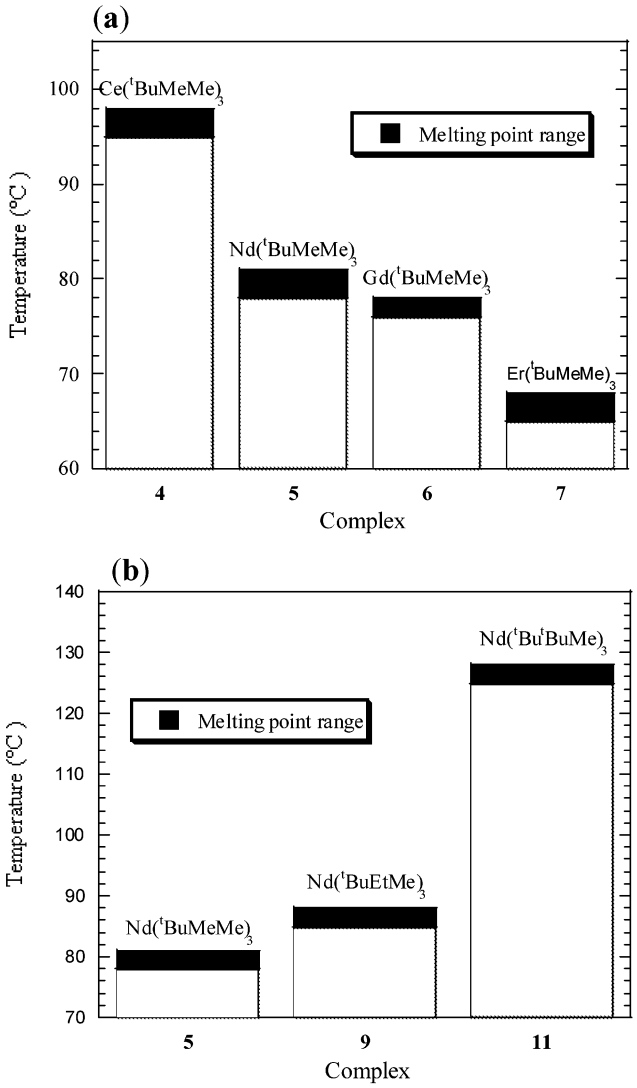

Figure 3. Melting point trends of β-ketoiminato lanthanide complexes as a function of (a) Ln^{3+} identity and (b) alkyl substituent at ligand imino R_2 site.

uents bulkier than a methyl group at the ether R_3 site were successful [i.e., Ln(tBuEtEt)$_3$ and Ln(MeMeEt)$_3$]; however, only qualitative assessment of physical characteristics was possible owing to the thick, viscous nature of the liquid products.

Precursor Molecular Structures. Single-crystal X-ray diffraction studies were carried out on lanthanide complexes **4**−**7**, **9**, **10**, and **12**. Important bond distances and angles for these structures are tabulated in Tables 5−8, and relevant lanthanide ionic radii are listed in Table 9. Generally, the crystal structures of the 8-coordinate Ce^{3+}, Nd^{3+}, and Gd^{3+} complexes [i.e., **4**, **5**, **6**, and **9**] reveal that two of the three ligands are coordinated to the metal through all three possible donor sites; however, the third ligand is bidentate, with a noncoordinating ether moiety (Figures 4 and 5, 6 and 7, 8 and 9, and 10 and 11, respectively). Conversely, the solid-state structures of Er^{3+} complexes **7** and **10** are 7-coordinate, with two dangling ether groups (Figures 12 and 13, and 14 and 15, respectively). The crystal structure of complex **12** reveals that this Er^{3+} compound is also 7-coordinate, although two ligands act as tridentate donors and the third is monodentate (Figures 16 and 17). Comparisons to known structures are made in the Discussion section.

Table 5. Selected Bond Lengths (Å) and Angles (deg) for Complexes **4** and **5**

4		**5**	
Ce(1A)−O(41A)	2.349(3)	Nd(1)−O(1)	2.278(1)
Ce(1A)−O(21A)	2.374(3)	Nd(1)−O(41)	2.289(1)
Ce(1A)−O(1A)	2.385(3)	Nd(1)−O(21)	2.315(9)
Ce(1A)−N(21A)	2.616(4)	Nd(1)−N(1)	2.518(9)
Ce(1A)−N(41A)	2.663(4)	Nd(1)−N(41)	2.568(1)
Ce(1A)−N(1A)	2.684(4)	Nd(1)−N(21)	2.582(1)
Ce(1A)−O(2A)	2.694(3)	Nd(1)−O(22)	2.649(8)
Ce(1A)−O(22A)	2.823(3)	Nd(1)−O(2)	2.813(9)
O(41A)−Ce(1A)−O(21A)	85.75(1)	O(1)−Nd(1)−O(41)	85.3(4)
O(41A)−Ce(1A)−O(1A)	147.42(1)	O(1)−Nd(1)−O(21)	121.8(4)
O(21A)−Ce(1A)−O(1A)	119.37(1)	O(41)−Nd(1)−O(21)	147.1(3)
O(41A)−Ce(1A)−N(21A)	87.26(1)	O(1)−Nd(1)−N(1)	70.9(3)
O(21A)−Ce(1A)−N(21A)	69.82(1)	O(41)−Nd(1)−N(1)	89.3(3)
O(1A)−Ce(1A)−N(21A)	83.22(1)	O(21)−Nd(1)−N(1)	83.7(3)
O(41A)−Ce(1A)−N(41A)	69.66(1)	O(1)−Nd(1)−N(41)	143.5(4)
O(21A)−Ce(1A)−N(41A)	143.31(1)	O(41)−Nd(1)−N(41)	70.9(3)
O(1A)−Ce(1A)−N(41A)	94.51(1)	O(21)−Nd(1)−N(41)	91.1(4)
N(21A)−Ce(1A)−N(41A)	132.61(1)	N(1)−Nd(1)−N(41)	133.6(3)
O(41A)−Ce(1A)−N(1A)	141.54(1)	O(1)−Nd(1)−N(21)	79.2(3)
O(21A)−Ce(1A)−N(1A)	80.30(1)	O(41)−Nd(1)−N(21)	139.8(3)
O(1A)−Ce(1A)−N(1A)	68.04(1)	O(21)−Nd(1)−N(21)	69.2(3)
N(21A)−Ce(1A)−N(1A)	120.19(1)	N(1)−Nd(1)−N(21)	119.3(4)
N(41A)−Ce(1A)−N(1A)	102.01(1)	N(41)−Nd(1)−N(21)	101.2(4)
O(41A)−Ce(1A)−O(2A)	79.79(1)	O(1)−Nd(1)−O(22)	73.5(3)
O(21A)−Ce(1A)−O(2A)	74.47(1)	O(41)−Nd(1)−O(22)	78.0(3)
O(1A)−Ce(1A)−O(2A)	124.62(1)	O(21)−Nd(1)−O(22)	124.6(3)
N(21A)−Ce(1A)−O(2A)	142.74(1)	N(1)−Nd(1)−O(22)	143.0(3)
N(41A)−Ce(1A)−O(2A)	74.67(1)	N(41)−Nd(1)−O(22)	74.7(3)
N(1A)−Ce(1A)−O(2A)	62.00(1)	N(21)−Nd(1)−O(22)	62.1(3)
O(41A)−Ce(1A)−O(22A)	77.28(1)	O(1)−Nd(1)−O(2)	129.9(3)
O(21A)−Ce(1A)−O(22A)	129.81(1)	O(41)−Nd(1)−O(2)	78.4(3)
O(1A)−Ce(1A)−O(22A)	70.66(1)	O(21)−Nd(1)−O(2)	69.9(3)
N(21A)−Ce(1A)−O(22A)	62.58(1)	N(1)−Nd(1)−O(2)	62.0(3)
N(41A)−Ce(1A)−O(22A)	72.01(1)	N(41)−Nd(1)−O(2)	72.9(3)
N(1A)−Ce(1A)−O(22A)	137.62(1)	N(21)−Nd(1)−O(2)	138.5(3)
O(2A)−Ce(1A)−O(22A)	144.41(1)	O(22)−Nd(1)−O(2)	144.7(3)

Precursor Volatility Trends. Several of the present lanthanide precursors were further characterized by vacuum thermogravimetric analysis (TGA) at pressures approximating those used in film growth. The new precursors were directly compared to commercially supplied Ce(dpm)$_4$ and Er(dpm)$_3$. Figure 11a shows the raw comparative weight loss versus temperature data for cerium complexes **4**, **8**, and Ce(dpm)$_4$. An Arrhenius analysis (sublimation rate versus inverse temperature; Figure 11b) for these Ce complexes allows direct comparison of the molar volatility/transport rate characteristics.[26] Finally, the Ce complexes were characterized in isothermal experiments (Figure 11c). Note that complex **4** exhibits the highest molar volatility under MOCVD reactor conditions (155 °C; lowest apparent activation energy; see Figure 11b). Similar plots are shown for Er complex **10** and Er(dpm)$_3$ (Figures 12a−c) and reveal that **10** has constant vaporization characteristics with little apparent thermal instability.

CeO_2 Film Growth Experiments. Epitaxial CeO_2 films were deposited in situ on (001)-oriented YSZ substrates using newly developed Ce precursor **4**, Ce(tBuMeMe)$_3$. The reservoir containing **4** was maintained at 150−160 °C, and Ar flowing at 70 sccm carried the precursor into the reactor hot zone, where it reacted with 100 sccm of O_2 to form the

Table 6. Selected Bond Lengths (Å) and Angles (deg) for Complexes **6** and **7**

6		**7**	
Gd(1)−O(1)	2.2362(2)	Er(1)−O(41)	2.193(3)
Gd(1)−O(3)	2.2773(2)	Er(1)−O(21)	2.195(3)
Gd(1)−O(10)	2.280(2)	Er(1)−O(1)	2.212(3)
Gd(1)−N(11)	2.537(2)	Er(1)−N(41)	2.437(3)
Gd(1)−N(1)	2.540(2)	Er(1)−N(1)	2.439(3)
Gd(1)−N(3)	2.549(2)	Er(1)−O(2)	2.465(3)
Gd(1)−O(2)	2.554(2)	Er(1)−N(21)	2.535(3)
Gd(1)−O(4)	2.7520(2)		
O(1)−Gd(1)−O(3)	144.22(7)	O(41)−Er(1)−O(21)	160.10(1)
O(1)−Gd(1)−O(10)	94.98(8)	O(41)−Er(1)−O(1)	114.88(1)
O(3)−Gd(1)−O(10)	111.39(7)	O(21)−Er(1)−O(1)	82.92(1)
O(1)−Gd(1)−N(11)	83.58(8)	O(41)−Er(1)−N(41)	76.33(1)
O(3)−Gd(1)−N(11)	82.14(7)	O(21)−Er(1)−N(41)	100.69(1)
O(10)−Gd(1)−N(11)	72.17(7)	O(1)−Er(1)−N(41)	76.88(1)
O(1)−Gd(1)−N(1)	72.70(7)	O(41)−Er(1)−N(1)	77.32(1)
O(3)−Gd(1)−N(1)	134.58(7)	O(21)−Er(1)−N(1)	118.18(1)
O(10)−Gd(1)−N(1)	78.25(7)	O(1)−Er(1)−N(1)	73.58(1)
N(11)−Gd(1)−N(1)	140.03(7)	N(41)−Er(1)−N(1)	126.66(1)
O(1)−Gd(1)−N(3)	95.57(7)	O(41)−Er(1)−O(2)	95.18(1)
O(3)−Gd(1)−N(3)	74.43(7)	O(21)−Er(1)−O(2)	81.01(1)
O(10)−Gd(1)−N(3)	148.87(7)	O(1)−Er(1)−O(2)	123.09(1)
N(11)−Gd(1)−N(3)	138.16(7)	N(41)−Er(1)−O(2)	159.86(1)
N(1)−Gd(1)−N(3)	77.12(7)	N(1)−Er(1)−O(2)	67.31(1)
O(1)−Gd(1)−O(2)	139.37(7)	O(41)−Er(1)−N(21)	87.04(1)
O(3)−Gd(1)−O(2)	74.39(7)	O(21)−Er(1)−N(21)	73.07(1)
O(10)−Gd(1)−O(2)	70.77(7)	O(1)−Er(1)−N(21)	145.90(1)
N(11)−Gd(1)−O(2)	124.15(7)	N(41)−Er(1)−N(21)	84.06(1)
N(1)−Gd(1)−O(2)	67.26(7)	N(1)−Er(1)−N(21)	139.33(1)
N(3)−Gd(1)−O(2)	82.29(7)	O(2)−Er(1)−N(21)	77.21(1)
O(1)−Gd(1)−O(4)	70.35(6)		
O(3)−Gd(1)−O(4)	73.88(6)		
O(10)−Gd(1)−O(4)	137.55(6)		
N(11)−Gd(1)−O(4)	66.84(7)		
N(1)−Gd(1)−O(4)	129.47(7)		
N(3)−Gd(1)−O(4)	73.51(6)		
O(2)−Gd(1)−O(4)	144.15(6)		

Table 7. Selected Bond Lengths (Å) and Angles (deg) for Complexes **9** and **10**

9		**10**	
Nd(1)−O(1B)	2.303(2)	Er(1)−O(1A)	2.185(2)
Nd(1)−O(1A)	2.304(2)	Er(1)−O(1C)	2.196(16)
Nd(1)−O(1C)	2.336(2)	Er(1)−O(1B)	2.199(16)
Nd(1)−N(5B)	2.543(2)	Er(1)−N(5B)	2.438(2)
Nd(1)−N(5A)	2.589(2)	Er(1)−N(5C)	2.445(2)
Nd(1)−N(5C)	2.647(2)	Er(1)−O(8C)	2.476(2)
Nd(1)−O(9C)	2.663(2)	Er(1)−N(5A)	2.559(2)
Nd(1)−O(8B)	2.758(2)		
O(1B)−Nd(1)−O(1A)	83.23(7)	O(1A)−Er(1)−O(1C)	83.78(6)
O(1B)−Nd(1)−O(1C)	122.76(7)	O(1A)−Er(1)−O(1B)	158.86(6)
O(1A)−Nd(1)−O(1C)	146.78(7)	O(1C)−Er(1)−O(1B)	113.67(6)
O(1B)−Nd(1)−N(5B)	70.93(7)	O(1A)−Er(1)−N(5B)	96.91(6)
O(1A)−Nd(1)−N(5B)	84.56(7)	O(1C)−Er(1)−N(5B)	78.32(6)
O(1C)−Nd(1)−N(5B)	85.43(7)	O(1B)−Er(1)−N(5B)	76.25(6)
O(1B)−Nd(1)−N(5A)	138.57(7)	O(1A)−Er(1)−N(5C)	120.21(7)
O(1A)−Nd(1)−N(5A)	70.37(7)	O(1C)−Er(1)−N(5C)	73.51(6)
O(1C)−Nd(1)−N(5A)	95.04(7)	O(1B)−Er(1)−N(5C)	77.89(6)
N(5B)−Nd(1)−N(5A)	134.22(7)	N(5B)−Er(1)−N(5C)	129.44(7)
O(1B)−Nd(1)−N(5C)	80.42(6)	O(1A)−Er(1)−O(8C)	81.72(6)
O(1A)−Nd(1)−N(5C)	141.40(7)	O(1C)−Er(1)−O(8C)	122.40(6)
O(1C)−Nd(1)−N(5C)	69.08(6)	O(1B)−Er(1)−O(8C)	97.37(6)
N(5B)−Nd(1)−N(5C)	121.75(7)	N(5B)−Er(1)−O(8C)	158.66(6)
N(5A)−Nd(1)−N(5C)	100.55(7)	N(5C)−Er(1)−O(8C)	67.06(6)
O(1B)−Nd(1)−O(9C)	74.11(6)	O(1A)−Er(1)−N(5A)	73.14(6)
O(1A)−Nd(1)−O(9C)	80.40(6)	O(1C)−Er(1)−N(5A)	147.69(6)
O(1C)−Nd(1)−O(9C)	123.85(6)	O(1B)−Er(1)−N(5A)	86.03(6)
N(5B)−Nd(1)−O(9C)	143.24(7)	N(5B)−Er(1)−N(5A)	82.29(6)
N(5A)−Nd(1)−O(9C)	70.51(6)	N(5C)−Er(1)−N(5A)	137.85(6)
N(5C)−Nd(1)−O(9C)	61.57(6)	O(8C)−Er(1)−N(5A)	76.93(6)
O(1B)−Nd(1)−O(8B)	130.29(6)		
O(1A)−Nd(1)−O(8B)	77.20(7)		
O(1C)−Nd(1)−O(8B)	70.11(6)		
N(5B)−Nd(1)−O(8B)	62.14(7)		
N(5A)−Nd(1)−O(8B)	75.01(6)		
N(5C)−Nd(1)−O(8B)	138.35(6)		
O(9C)−Nd(1)−O(8B)	143.54(6)		

desired films. The overall working pressure was 3.5 Torr. Epitaxial films were successfully obtained at susceptor temperatures ranging between 450 and 650 °C, and the effects of temperature variation on film microstructure were closely examined (vide infra). Film thickness varied between ∼100 and 200 nm, with a dependence on growth temperature (vide infra).

CeO_2 Film Characterization. A typical $\theta-2\theta$ X-ray diffraction pattern of an as-grown CeO_2 film (Figure 13a) consists of only CeO_2 and substrate (00*l*) reflections. The intensity of diffraction from films grown for a fixed time (3.5 h) was found to decrease with increasing deposition temperature, and diffraction from CeO_2 films deposited at 650 °C is quite weak. The film out-of-plane orientation characteristics were analyzed by an ω-rocking scan of the (002) reflection, and the fwhm, determined by least-squares fitting, was found to decrease from 1.0° to 0.2° with increasing deposition temperature (450−650 °C). The ω-rocking curves of the films grown at high temperature (>520 °C) are in fact a superposition of a broad underlying peak with a narrow one sitting on top. With increase of deposition temperature, the narrow component tends to dominate. The ω scan fwhm from the CeO_2 films deposited at 540 °C is 0.85° (Figure 13b).

XRD ϕ scans were performed to assess the quality of the in-plane epitaxy. Four equivalent planes of reflection are observed, repeating every 90° and in the same positions as those from the YSZ substrates (Figure 13c), demonstrating a high level of in-plane epitaxy. The fwhm from the ϕ scan of {113} CeO_2 is 1.65°. From the $\theta-2\theta$ and ϕ XRD scans, the orientation relationship between the film and the YSZ substrate is therefore CeO_2 (001)[$\bar{1}$10]//YSZ (001)[$\bar{1}$10]. AFM images of the as-grown CeO_2 films show that the surfaces consist of a granular structure. At low-growth temperatures (450 °C), the tetragonal-pyramidal shaped hillock-type grains have sizes in the range 50−110 nm, while the rms roughness is about 15.5 Å (Figure 14a). At higher growth temperatures (above 540 °C), the surface becomes much smoother (rms roughness ∼ 4.3 Å), and hillock surface features are not detectable (Figure 14b).

Cross-sectional high-resolution electron microscopy (HREM) was also used to investigate the epitaxial growth of the CeO_2 films on the (001) YSZ substrates. The CeO_2 film grown at 540 °C exhibits sizable regions of single crystal, defect-free and epitaxial growth (Figure 15). HREM images and selected area diffraction (Figure 16) also reveal that the CeO_2 films and the YSZ substrates have the same orientational relationship as that defined by the XRD experiments (vide supra). The interface area between the CeO_2 and YSZ substrates contains atomic stacking dislocations having a periodicity of ∼44 Å. As the deposition temperature increases, the columnar size remains almost

Table 8. Selected Bond Lengths (Å) and Angles (deg) for Complex **12**

Er(1)−O(1C)	2.165(1)	O(8B)−C(7B)	1.429(3)
Er(1)−O(1A)	2.173(1)	N(5B)−C(4B)	1.314(3)
Er(1)−O(1B)	2.201(2)	N(5B)−C(6B)	1.469(3)
Er(1)−N(5A)	2.415(2)	C(2B)−C(3B)	1.385(3)
Er(1)−N(5B)	2.448(2)	C(2B)−C(10B)	1.540(3)
Er(1)−O(8B)	2.478(2)	C(3B)−C(4B)	1.432(3)
Er(1)−O(8A)	2.484(2)	C(4B)−C(14B)	1.563(3)
O(1A)−C(2A)	1.300(2)	C(6B)−C(7B)	1.512(4)
O(8A)−C(9A)	1.435(3)	O(1C)−C(2C)	1.319(2)
O(8A)−C(7A)	1.437(3)	O(8C)−C(9C)	1.409(3)
N(5A)−C(4A)	1.308(3)	O(8C)−C(7C)	1.419(3)
N(5A)−C(6A)	1.467(3)	N(5C)−C(4C)	1.277(3)
C(2A)−C(3A)	1.374(3)	N(5C)−C(6C)	1.450(3)
C(2A)−C(10A)	1.535(3)	C(2C)−C(3C)	1.352(3)
C(3A)−C(4A)	1.437(3)	C(2C)−C(10C)	1.544(3)
C(4A)−C(14A)	1.565(3)	C(3C)−C(4C)	1.470(3)
C(6A)−C(7A)	1.509(4)	C(4C)−C(14C)	1.542(3)
O(1B)−C(2B)	1.275(3)	C(6C)−C(7C)	1.513(3)
O(8B)−C(9B)	1.423(3)		

O(1C)−Er(1)−O(1A)	98.84(6)	O(1A)−Er(1)−O(8B)	77.83(5)
O(1C)−Er(1)−O(1B)	176.56(6)	O(1B)−Er(1)−O(8B)	102.69(6)
O(1A)−Er(1)−O(1B)	82.69(6)	N(5A)−Er(1)−O(8B)	150.64(6)
O(1C)−Er(1)−N(5A)	90.58(6)	N(5B)−Er(1)−O(8B)	66.64(6)
O(1A)−Er(1)−N(5A)	75.91(6)	O(1C)−Er(1)−O(8A)	90.01(5)
O(1B)−Er(1)−N(5A)	86.80(6)	O(1A)−Er(1)−O(8A)	143.04(6)
O(1C)−Er(1)−N(5B)	107.74(6)	O(1B)−Er(1)−O(8A)	86.94(6)
O(1A)−Er(1)−N(5B)	130.48(6)	N(5A)−Er(1)−O(8A)	68.14(6)
O(1B)−Er(1)−N(5B)	73.24(6)	N(5B)−Er(1)−O(8A)	78.90(6)
N(5A)−Er(1)−N(5B)	142.28(6)	O(8B)−Er(1)−O(8A)	139.13(5)
O(1C)−Er(1)−O(8B)	80.68(6)		

Table 9. Average Lanthanide−Ligand Atom Bond Distances and Bond Distance Trends (Å) for Complexes **4**−**7**, **9**, **10**, and **12**

complex	coord no.	Ln^{3+} ionic radius[a]	Ln−O(keto)	Ln−N(imino)	Ln−O(ether)
4, Ce(^{t}BuMeMe)$_3$	8	1.143	2.371(6)	2.655(2)	2.760(3)
5, Nd(^{t}BuMeMe)$_3$	8	1.109	2.294(4)	2.556(4)	2.731(9)
6, Gd(^{t}BuMeMe)$_3$	8	1.053	2.264(6)	2.543(9)	2.653(1)
7, Er(^{t}BuMeMe)$_3$	7	0.945	2.200(3)	2.470(6)	2.465(3)
9, Nd(^{t}BuEtMe)$_3$	8	1.109	2.314(5)	2.593(2)	2.710(7)
10, Er(^{t}BuEtMe)$_3$	7	0.945	2.194(2)	2.480(7)	2.476(2)
12, Er(^{t}Bu^{t}BuMe)$_3$	7	0.945	2.180(1)	2.432(2)	2.481(2)
Ce^{3+} av	8	1.143	2.371(6)	2.655(2)	2.760(3)
Nd^{3+} av	8	1.109	2.304(5)	2.574(8)	2.721(3)
Gd^{3+} av	8	1.053	2.264(6)	2.543(9)	2.653(1)
Er^{3+} av	7	0.945	2.191(5)	2.461(2)	2.474(2)

[a] Ionic radii for corresponding coordination number.[74]

unchanged but the film surface becomes smoother. Film thickness was also ascertained from cross-sectional TEM samples. With an increase in deposition temperature, the CeO_2 growth rate decreases slightly from ~10 Å/min at 450 °C to ~6.5 Å/min at 540 °C.

Despite the columnar structure, the present CeO_2 films are very dense, and no fissures are evident either at the interface or within the film (Figure 15). In fact, the column boundaries are difficult to observe in the HREM. In contrast, the YSZ substrates are found not to be atomically smooth. On the step planes, the CeO_2 films grow with an atomically abrupt interface. However, at the YSZ step edges, slight bending of crystal planes parallel to the substrate surfaces (arrow 1 in Figure 15) formed near the step. Simultaneously, slight bending of the crystal planes parallel to the substrate surface, indicated by arrow 2 in Figure 15, can also be observed near the columnar boundaries in the films.

YBCO Film Growth on MOCVD-Derived CeO_2 Buffer Layers. Well-aligned YBCO films were successfully deposited by the pulsed MOCVD POMBE[101] technique on the present low-temperature (540 °C) MOCVD-derived epitaxial CeO_2 films. XRD $\theta-2\theta$ data for the YBCO film deposition, shown in Figure 17a, consists of bilayer film features with *c*-axis oriented YBCO growth on the CeO_2 film. The ω scan fwhm of the YBCO films is 0.80° for the (005) reflection (inset, Figure 17a). In ϕ scans on the present specimens, four equivalent (102) YBCO planes of reflection are observed, repeating every 90° (Figure 17b). The fwhm from the ϕ scan of the {102} YBCO planes is as narrow as 1.30. Four-probe transport measurements on these multilayer structures reveal a transition temperature of 86.5 K (transition width ~ 2.0 K; Figure 18a). The critical current density at 77.4 K is 1.08×10^6 A/cm^2, as shown in Figure 18b.

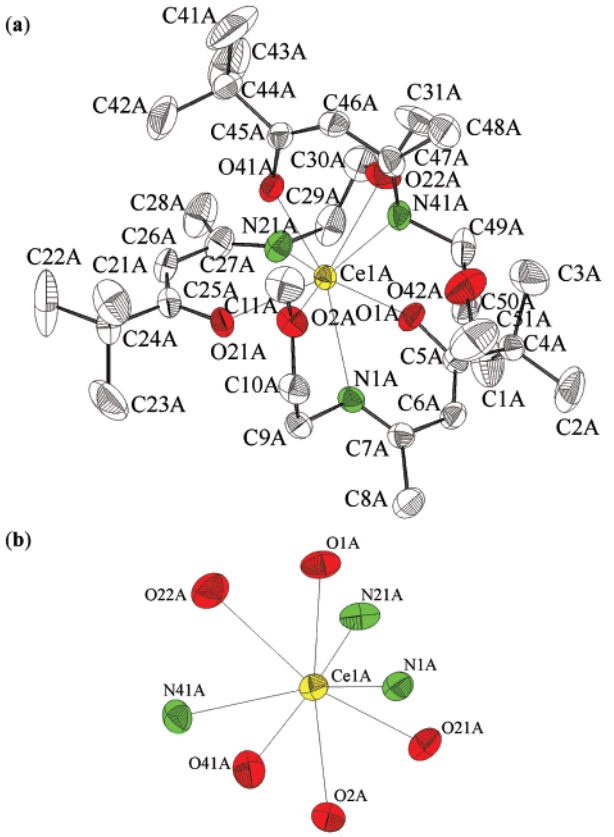

Figure 4. (a) Solid-state crystal structure of 8-coordinate cerium complex **4**, Ce(^{t}BuMeMe)$_3$. (b) Immediate coordination environment of 8-coordinate cerium complex **4**, Ce(^{t}BuMeMe)$_3$.

Discussion

The present synthetic coordination chemistry and film growth study was undertaken to develop a new class of lanthanide MOCVD precursors that would be thermally stable, volatile, fluorine-free, and liquid at typical reservoir temperatures for useful oxide growth conditions. No existing commercial or previously synthesized precursor in the published literature possesses all of these qualifications. The discussion below shows that the broad new class of lanthanide β-ketoiminate complexes reported here satisfies all of the desired characteristics and proves to be suitable for oxide MOCVD, as demonstrated by growth of high-quality CeO_2 thin films and their implementation as buffer layers for the growth of high-quality YBCO films.

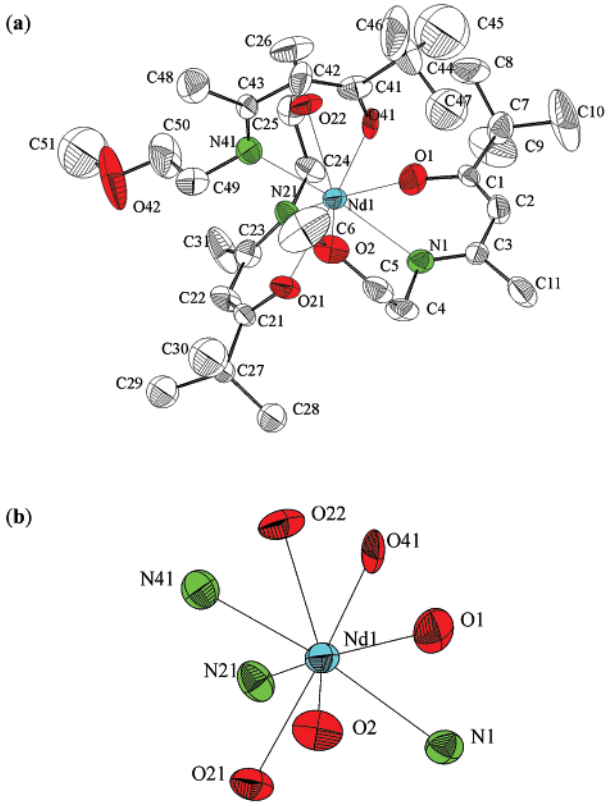

Figure 5. (a) Solid-state crystal structure of 8-coordinate neodymium complex **5**, Nd(^{t}BuMeMe)$_3$. (b) Immediate coordination environment of 8-coordinate neodymium complex **5**, Nd(^{t}BuMeMe)$_3$.

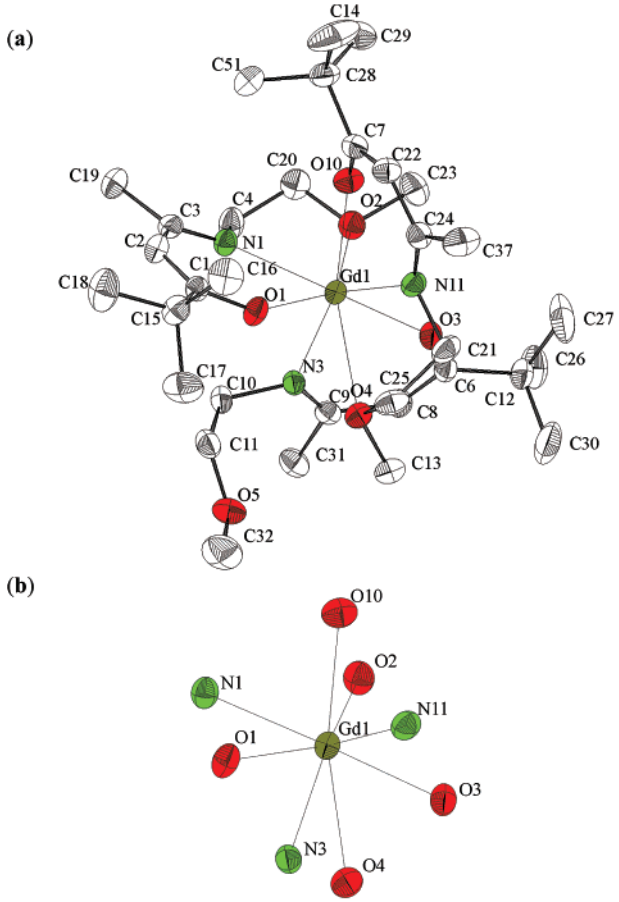

Figure 6. (a) Solid-state crystal structure of 8-coordinate gadolinium complex **6**, Gd(^{t}BuMeMe)$_3$. (b) Immediate coordination environment of 8-coordinate gadolinium complex **6**, Gd(^{t}BuMeMe)$_3$.

Precursor Synthesis, Structures, and Properties. The one-pot syntheses of the present ether-functionalized lanthanide β-ketoiminate complexes are uncomplicated, and isolation by in vacuo removal of the $HN(SiMe_3)_2$ byproduct followed by recrystallization of the crude material from pentane is straightforward. The waxy solids obtained (Figure 2) are characteristically highly colored, display melting points below those reported for commonly used β-diketonate precursors,[102] and can be sublimed at suitably low temperatures (80−110 °C) under reduced pressure (10^{-4} Torr). Additionally, substitution of various alkyl moieties on the β-ketoiminate ligand backbone allows tailoring of the β-ketoiminate melting point, as summarized in Table 4. The observed melting point decreases across the lanthanide series for a given ligand system [i.e., for the Ln(^{t}BuMeMe)$_3$ series: mp **4**, 95−98 °C; **5**, 78−81 °C; **6**, 76−78 °C; **7**, 65−68 °C; see Figure 3a], a manifestation of the lanthanide contraction. This melting point trend is also observed for the lanthanide β-diketonates, Ln(dpm)$_3$.[102] Substitution of an alkyl group with greater steric bulk at the imino location R_2 (e.g., ethyl or *tert*-butyl for methyl) leads to a higher melting point (i.e., mp **5**, 78−81 °C; **9**, 85−88 °C; **11**, 125−128 °C; see Figure 3b). It can be speculated that a greater R_1 to R_2 size disparity (i.e., R_1 = ^{t}Bu, R_2 = Me versus R_1 = ^{t}Bu, R_2 = Et or ^{t}Bu) lowers the symmetry of the complex, affording a lower-melting precursor.

Single-crystal X-ray diffraction experiments reveal that all lanthanide complexes formed with the present β-ketoiminate ligands are monomeric, a characteristic preferred for optimum volatility (Figures 4−17). In fact, the three potentially tridentate ligands exceed the coordinative demands of the Ln^{3+} ion in all cases studied (Ln^{3+} = Ce^{3+}, Nd^{3+}, Gd^{3+}, Er^{3+}), resulting in 8-coordinate complexes for Ce, Nd, and Gd (**4**, **5**, **6**, and **9**; Figures 4 and 5, 6 and 7, 8 and 9, and 10 and 11, respectively), compared to 7-coordinate Er compounds (**7**, **10**, and **12**; Figures 12 and 13, 14 and 15, and 16 and 17). This difference is doubtless a result of the lanthanide contraction, with the smaller Er^{3+} ion being coordinatively saturated at a lower coordination number. All the 8-coordinate structures display two ligands acting in tridentate fashion, with the third being bidentate with a noncoordinating ether group, consistent with the ether functionality being the only neutrally charged donor site.

Further of note is the anomalous solid-state structure of Er complex **12** (Figure 16), in which two of the three ligands act as tridentate donors, while the third is only monodentate, having both noncoordinating imino and ether components. This is in contrast to the other Er structures (**7** and **10**; Figures 12 and 13, and 14 and 15, respectively), which display one tridentate ligand and two bidentate ligands with dangling ether moieties, a bonding scheme similar to that observed

(102) Eisentraut, K. J.; Sievers, R. E. *J. Am. Chem. Soc.* **1965**, *87*, 5254−5256.

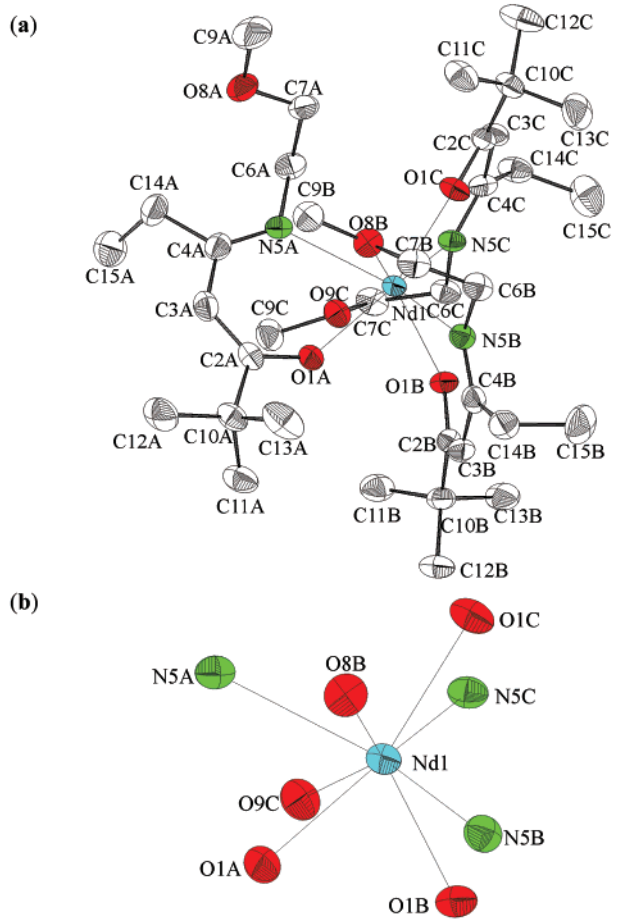

Figure 7. (a) Solid-state crystal structure of 8-coordinate neodymium complex **9**, Nd(^{t}BuEtMe)$_3$. (b) Immediate coordination environment of 8-coordinate neodymium complex **9**, Nd(^{t}BuEtMe)$_3$.

for the 8-coordinate Ce^{3+}, Nd^{3+}, and Gd^{3+} complexes (vide supra). The increased steric bulk of a *tert*-butyl group at the ligand imino site R_2 apparently restricts the "bite" of the charged β-ketoimine portion of this ligand. Close examination of the bond distances for complex **12** (Table 8, Figure 19) indicates that the intraligand metrical parameter trends are consistent with Er^{3+} coordination, since the keto oxygen-to-carbon bond length is longer, and the imino nitrogen-to-carbon bond length is shorter for the monodentate ligand than for the other two (tridentate) ligands.

Important bond distances and angles for all structures analyzed in this study (complexes **4**−**7**, **9**, **10**, and **12**) are compiled in Tables 5−8. Average bond distance values and bond distance trends based on lanthanide identity are compiled in Table 9. In all cases (Ln = Ce, Nd, Gd, Er), the Ln−O(keto) bond length is shorter than the Ln−O(ether) distance, consistent with the fact that the keto oxygen atom is a component of the anionic β-ketoiminato ligand fragment while the ether oxygen atom is a neutrally charged pendant donor. Additionally, the trend across the lanthanide series is for all Ln−O and Ln−N bond distances to decrease as the Ln^{3+} ion becomes heavier, an obvious manifestation of the lanthanide contraction. Variation in ligand substitution pattern effects only minor deviations in bond distances for a particular Ln^{3+} ion.

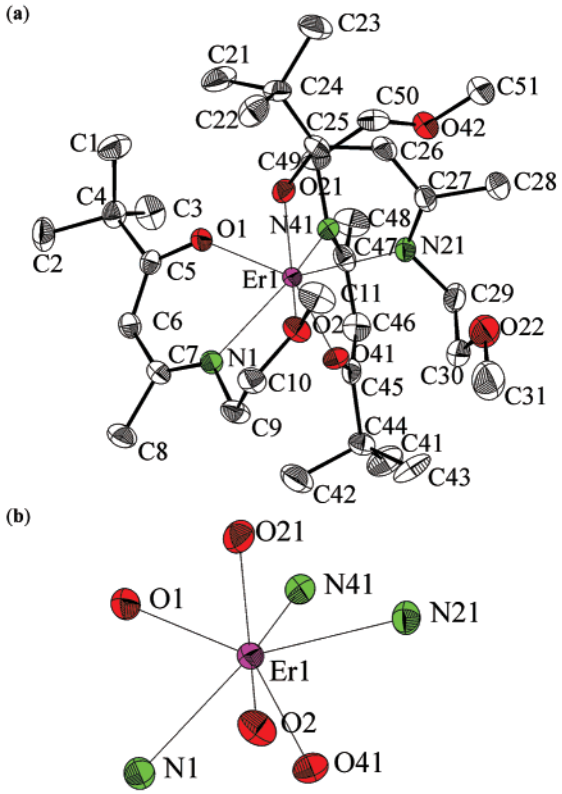

Figure 8. (a) Solid-state crystal structure of 7-coordinate erbium complex **7**, Er(^{t}BuMeMe)$_3$. (b) Immediate coordination environment of 7-coordinate erbium complex **7**, Er(^{t}BuMeMe)$_3$.

The average bond distances observed in Ce structure **4** (Table 9) can be compared to those reported for the 8-coordinate cerium of the dimer $Ce_2(etbd)_6(tetraglyme)$ (**IX**).[64] The average Ce−O(keto) bond length of **4** [2.371(6)

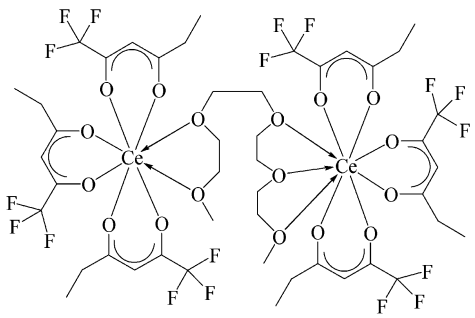

IX

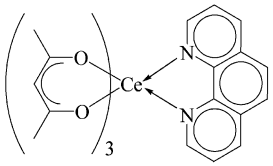

X

Å] is slightly shorter than that of **IX** [2.440(4) Å], while the average Ce−O(ether) bond length is longer [2.760(3) vs 2.605(0) Å]. This result is not surprising, in that fluorinated ligands are known to induce tighter binding of polyether oxygens, owing to greater induced electrophilicity at the

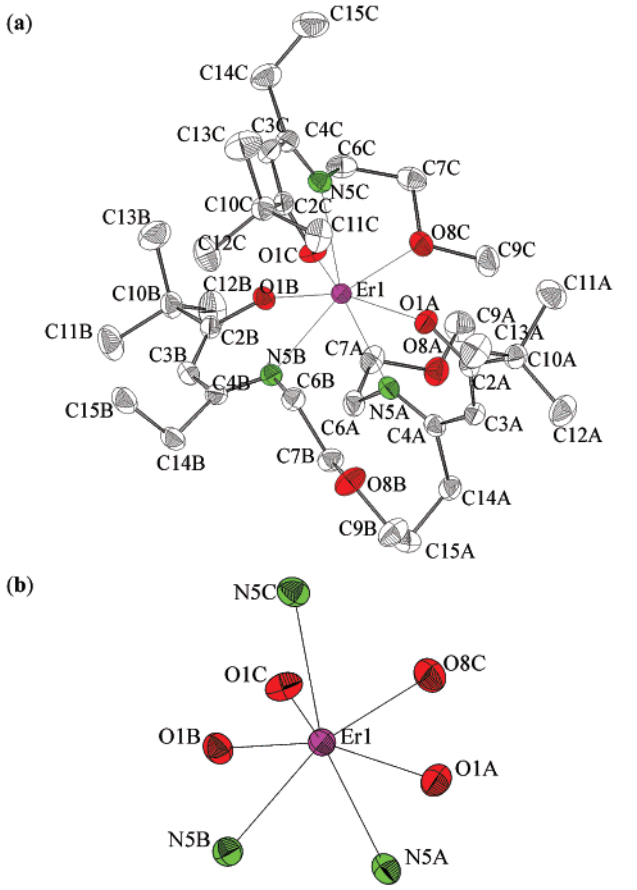

Figure 9. (a) Solid-state crystal structure of 7-coordinate erbium complex **10**, Er(^{t}BuEtMe)$_3$. (b) Immediate coordination environment of 7-coordinate erbium complex **10**, Er(^{t}BuEtMe)$_3$.

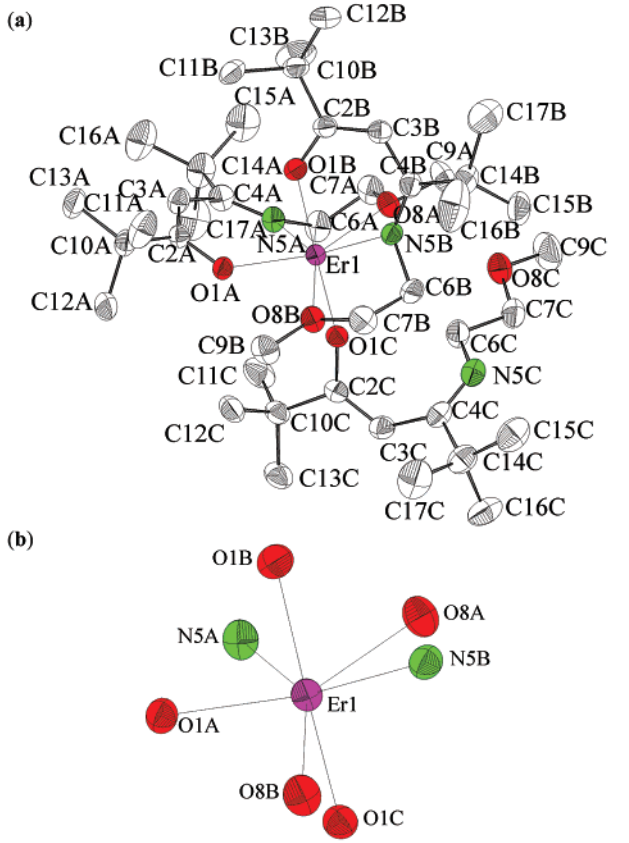

Figure 10. (a) Solid-state crystal structure of 7-coordinate erbium complex **12**, Er(^{t}Bu^{t}BuMe)$_3$. (b) Immediate coordination environment of 7-coordinate erbium complex **12**, Er(^{t}Bu^{t}BuMe)$_3$.

metal center. Complex **4** can also be compared to the reported structure of 8-coordinate Ce(acac)$_3$(phenanthroline) (**X**).[103] Here the average Ce−O(keto) bond length is 2.464(2) Å, longer than that of **4** [2.371(6) Å], and the average Ce−N bond length of 2.741(5) Å is comparable to that of complex **4** [2.760(3) Å].

The average Gd−O bond lengths in Gd complex **6** [Gd−O(keto), 2.264(6) Å; Gd−O(ether), 2.543(9) Å, Table 9] can be compared to those in complex **XI**. This Gd(dpm)$_3$-

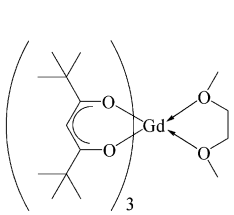

XI

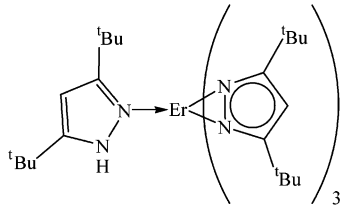

XII

(monoglyme) compound[62] has a longer average Gd−O(keto) bond length [2.333(4) Å] and a bit longer average Gd−O(ether) bond length [2.575(2) Å]. Clearly, the β-ketoiminate ligand of complex **6** is more tightly bound through the oxygen atoms to Gd^{3+} than in the β-diketonate/glyme ligand combination of complex **XI**. Perhaps directly appending the ether moiety to the β-ketoiminate backbone renders this ligand more compact, resulting in the shorter average bond lengths observed for **6**.

The overall average Er−O(keto) and Er−O(ether) bond distances (averaged values for complexes **7**, **10**, and **12**; Table 9) are 2.191(5) and 2.461(2) Å, respectively. The average Er−N bond distance for the present three complexes (**7**, **10**, and **12**) of 2.474(2) Å can be compared to those in structure **XII**.[53] Here the η^2-pyrazolato nitrogen atoms bind at a shorter average Er−N distance of 2.296(4) Å.

From the foregoing discussions, it is not surprising that introduction of alkyl substituents with greater steric bulk at the ether R_3 ligand site lowers the precursor melting point dramatically, judging from the fact that at least one of three possible ether components is not coordinated to the metal center in all cases characterized by X-ray diffraction, and from the symmetry-breaking arguments advanced above. Complexes of the type Ln(^{t}BuEtEt)$_3$ and Ln(MeMeEt)$_3$ (substitution of ethyl for methyl at R_3) were also synthesized in this study; however, attempts to purify the resulting viscous liquids were unsuccessful. Qualitatively, these crude complexes are lower-melting than the crude products obtained for complexes **4**−**12** as discussed above. Note that a precursor which exists in the liquid state at room temperature is *undesirable* because of difficulties in manipulation and transfer. Complexes **4**−**12** display optimum melting points, affording room-temperature solids that can easily be weighed and transferred to MOCVD precursor reservoirs, while also

(103) Christidis, P. C.; Tossidis, I. A.; Paschalidis, D. G.; Tzavellas, L. C. *Acta Crystallogr.* **1998**, *C54*, 1233−1236.

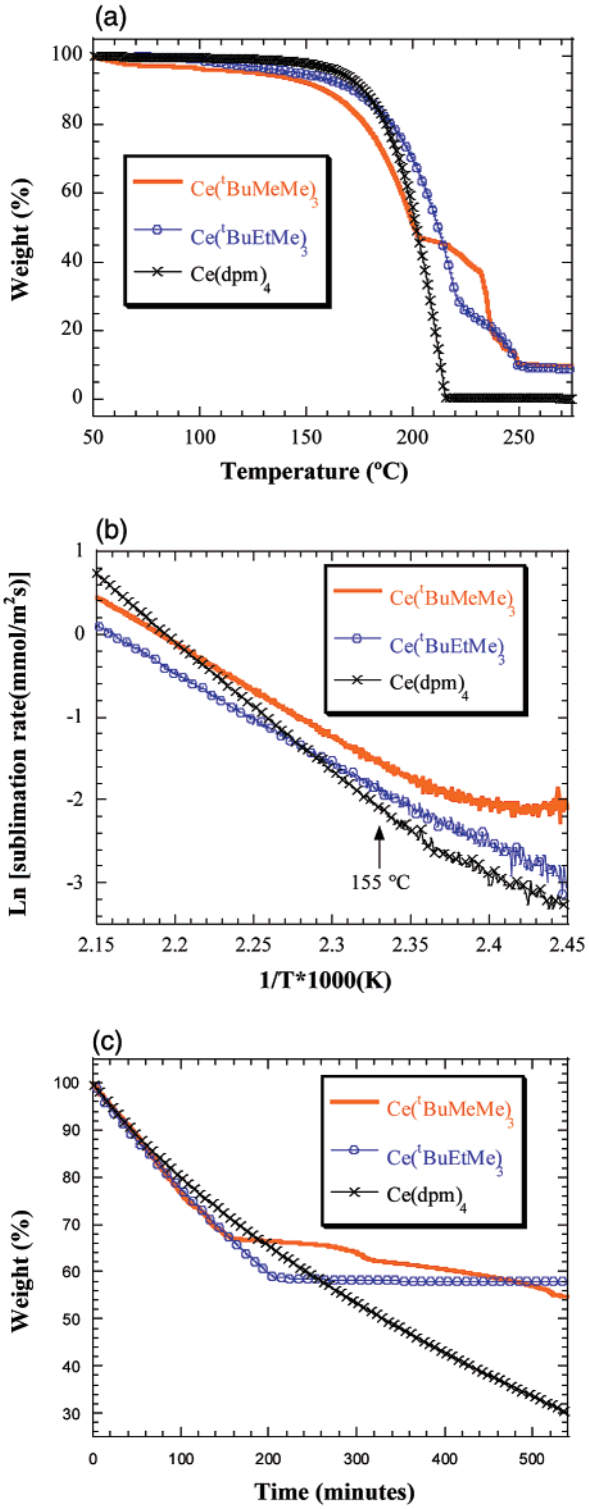

Figure 11. (a) Weight loss TGA volatility comparison between the new precursors Ce(^{t}BuMeMe)$_3$ (**4**) and Ce(^{t}BuEtMe)$_3$ (**8**), and commercially available Ce(dpm)$_4$. Data were collected at a ramp rate of 1.5 °C/min under 5.0 (± 0.1) Torr of N_2. (b) Thermal activation TGA plot showing direct volatility comparison between the new precursors Ce(^{t}BuMeMe)$_3$ (**4**) and Ce(^{t}BuEtMe)$_3$ (**8**), and commercially available Ce(dpm)$_4$. Data were collected at a ramp rate of 1.5 °C/min under 5.0 (± 0.1) Torr of N_2. Arrow points to experimental MOCVD reservoir temperature used for precursor **4**. (c) Isothermal TGA data comparing volatility of the new precursors Ce(^{t}BuMeMe)$_3$ (**4**) and Ce(^{t}BuEtMe)$_3$ (**8**), and commercially available Ce(dpm)$_4$. Data were collected at 155 °C under 5.0 (± 0.1) Torr of N_2.

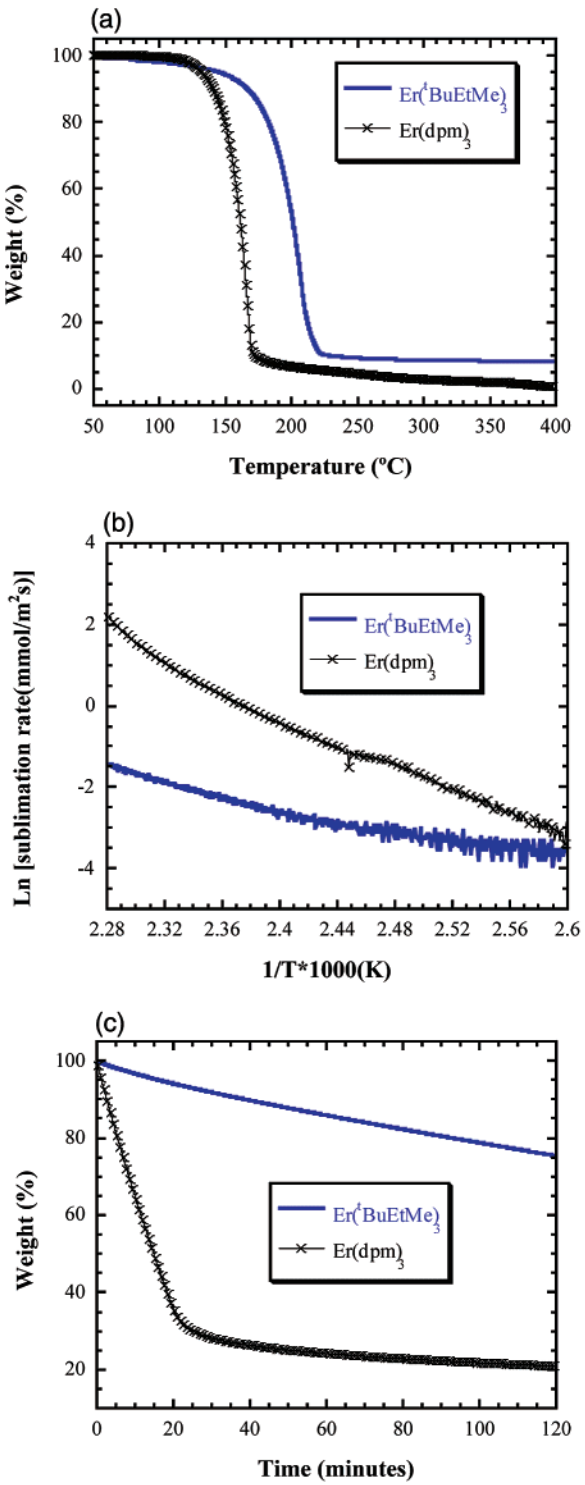

Figure 12. (a) Weight loss TGA volatility comparison between the new precursor Er(^{t}BuEtMe)$_3$ (**10**) and commercially available Er(dpm)$_3$. Data were collected at a ramp rate of 1.5 °C/min under 5.0 (± 0.1) Torr of N_2. (b) Thermal activation TGA plot showing direct volatility comparison between the new precursors Er(^{t}BuEtMe)$_3$ (**10**) and commercially available Er(dpm)$_3$. Data were collected at a ramp rate of 1.5 °C/min under 5.0 (± 0.1) Torr of N_2. (c) Isothermal TGA data showing volatility comparison between the new precursor Er(^{t}BuEtMe)$_3$ (**10**) and commercially available Er(dpm)$_3$. Data were collected at 155 °C under 5.0 (± 0.1) Torr of N_2.

melting at low temperatures to allow liquid-state operation and constant delivery into the reactor during film growth.

Thermogravimetric analysis (TGA) of the new β-ketoiminate precursors gives insight into volatility characteristics, since these analyses are carried out at a typical experimental MOCVD reactor pressure [5.0 (± 0.1) Torr]. Ce complexes

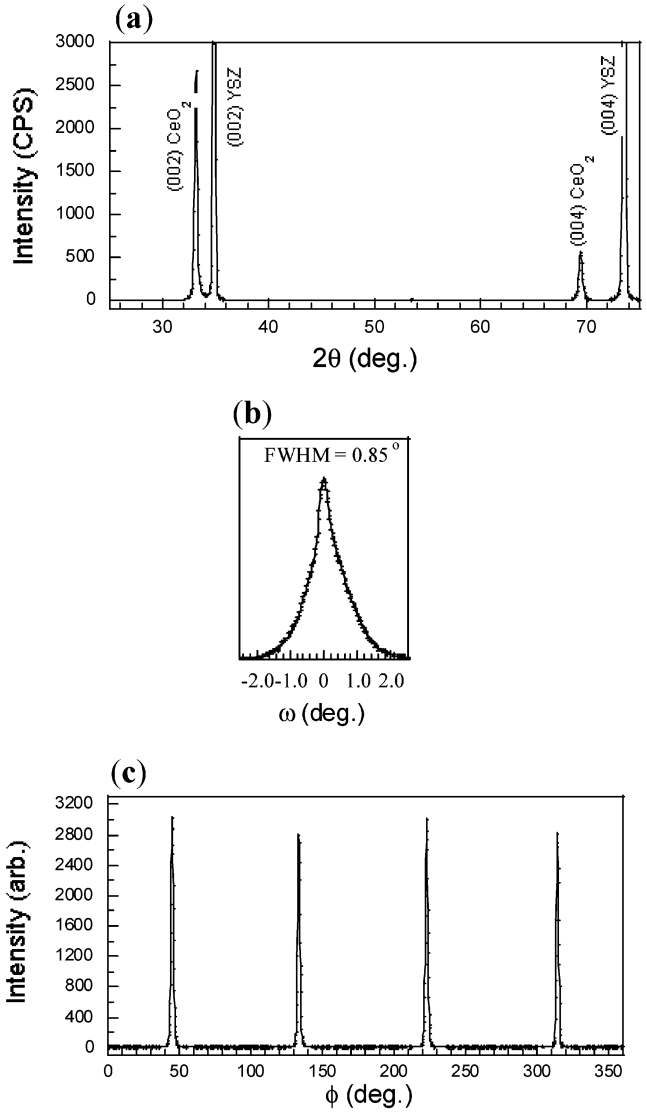

Figure 13. XRD of a 540 °C MOCVD-derived CeO_2 film grown on (001) YSZ: (a) $\theta-2\theta$ scan showing only (*00l*) reflections of both the film and substrate; (b) ω-rocking curve of the (002) reflection showing the film to have a high degree of out-of-plane epitaxy; (c) ϕ scan of the {113} peak revealing that the film has a high degree of in-plane microstructural alignment.

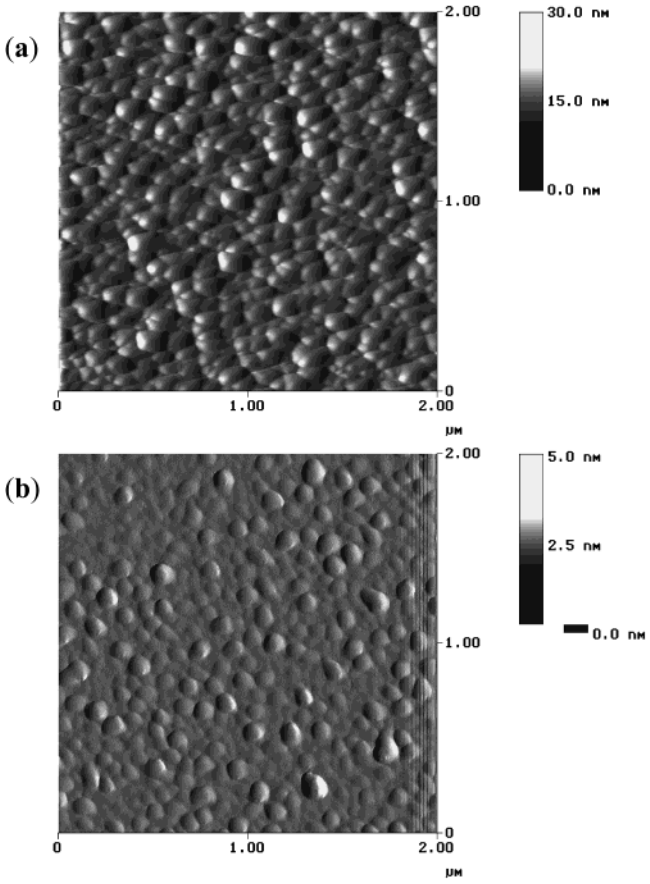

Figure 14. AFM images over a $2 \times 2\ \mu m^2$ area of CeO_2 films grown at (a) 450 °C, with an rms roughness of ~15.5 Å, and (b) 540 °C, with an rms roughness of ~4.3 Å.

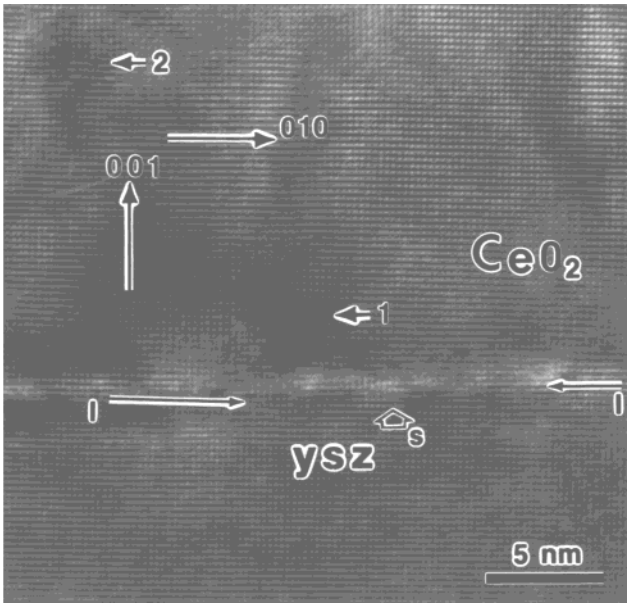

Figure 15. HREM image of the CeO_2/YSZ interface. Solid arrows mark the bent planes; open arrow points to the step on the substrate surface; "I" is for interface.

4 and **8** and Er complex **10** were directly compared with commercially available $Ce(dpm)_4$ and $Er(dpm)_3$. Figure 11a presents the weight-loss data for the Ce complexes, and although **4** and **8** appear to sublime with ~8% residue, we believe that this is a result of unavoidable exposure to ambient atmosphere during TGA handling. The thermal activation plot of sublimation rate is more directly related to MOCVD reactor behavior, and these data show that **4** and **8** clearly have substantially higher vaporization rates under typical film growth conditions and at lower temperatures than does $Ce(dpm)_4$, a characteristic preferred for optimum film growth (Figure 11b). The isothermal data (Figure 11c) reveal that all three Ce complexes show some degree of depressed volatility over time.

TGA weight-loss data for Er complex **10** and $Er(dpm)_3$ show that both complexes have favorable volatility characteristics, with the new complex subliming with a small amount of residue (as in the Ce case), most likely due to ambient-air exposure (Figure 12a). The thermal activation plot (Figure 12b) reveals that both Er complexes provide stable transport characteristics. Most significantly, the isothermal data show that **10** exhibits a stable evaporation rate, while $Er(dpm)_3$ sublimes more quickly initially, but then

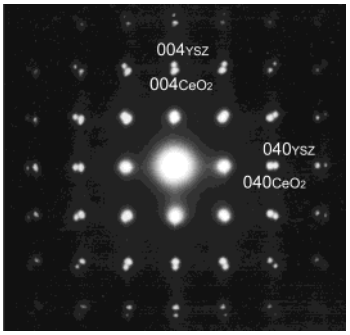

Figure 16. Composite electron diffraction pattern of CeO_2/YSZ.

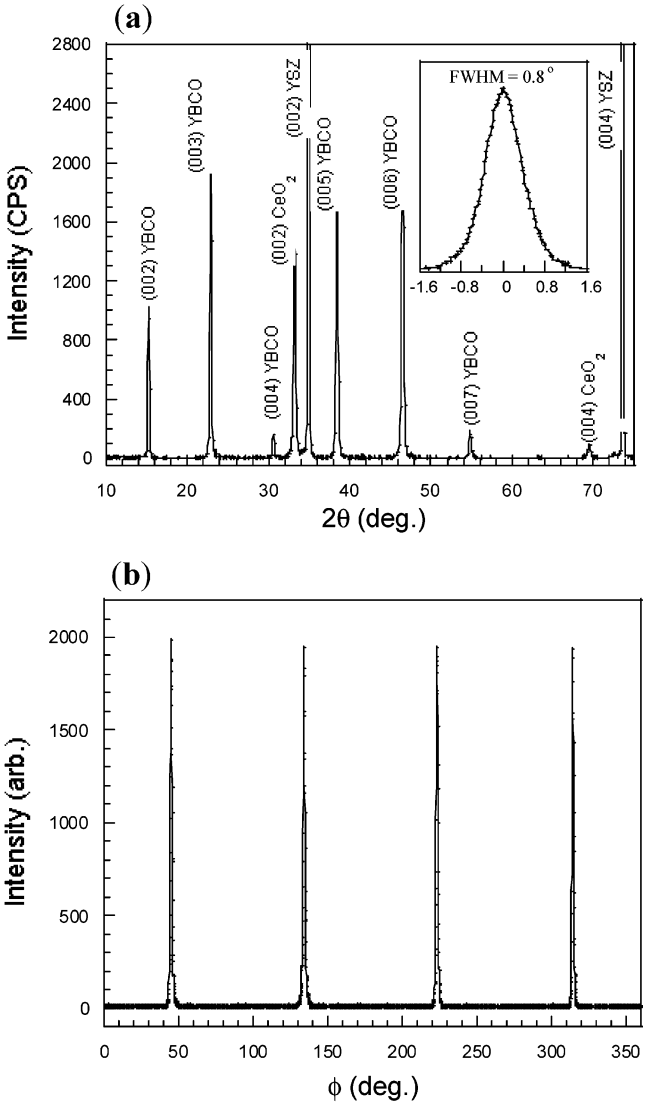

Figure 17. XRD of a YBCO/CeO_2/YSZ(001) multilayer structure: (a) $\theta-2\theta$ scan pattern; inset displays the ω-rocking curve of the (005) YBCO reflection, revealing good out-of-plane epitaxy; (b) ϕ scan of the {102} YBCO reflection showing excellent in-plane alignment.

displays a sudden fall in transport rate (Figure 12c). The superior MOCVD precursor is certainly one that provides a constant transport rate, as this implies stable delivery of the metal-containing species into the reactor hot-zone, hence compositionally reproducible thin film growth.

CeO_2 Film Growth. Buffer layers suitable for superconducting current-carrying applications must meet stringent

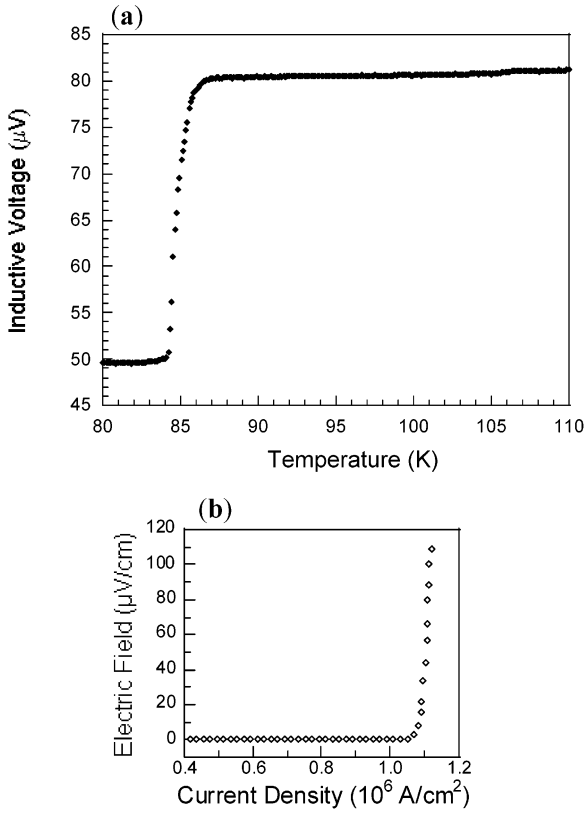

Figure 18. (a) T_c (with a transition width of ~2.0 K) and (b) J_c measurements on an YBCO/CeO_2/YSZ(001) multilayer.

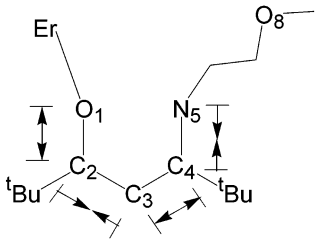

Distance	tridentate ligands (avg) (Å)	monodentate ligand (Å)
$O_1 - C_2$	1.288	1.319 (longer)
$C_2 - C_3$	1.380	1.352 (shorter)
$C_3 - C_4$	1.435	1.470 (longer)
$C_4 - N_5$	1.311	1.277 (shorter)

Figure 19. Schematic of the monodentate ligand of complex **12**. Arrows and the table express the comparative shortening and lengthening of the monodentate ligand bonds as compared to the two tridentate ligands of complex **12**.

orientation and processing requirements. Thus, the present CeO_2 films grown in situ at 450−650 °C by MOCVD were subjected to a battery of microstructural characterization techniques to assess crystalline quality. The XRD $\theta-2\theta$ diffraction pattern (Figure 13a) shows that the films consist of only (00*l*) oriented components on single-crystal (001) YSZ substrates. Such orientation is critical for subsequent deposition of a highly conductive (001)-oriented superconducting layer. A decrease in the XRD peak intensity is observed as the growth temperature is increased. The full-width-at-half-maximum (fwhm) of the ω scan assays the alignment/perfection of the film growth plane with respect to the substrate surface. In this case, the ω-rocking curve fwhm of the (002) reflection decreases from 1.0° to 0.2° with

increasing growth temperature. These values are comparable to those of films grown at considerably higher temperatures.[46,47,93] The higher-temperature film growth ω scan actually consists of a superposition of a narrow peak on top of a broader one, and the narrow component dominates as the temperature increases, which suggests thinner films.[46,93] This observation, together with the deposition temperature dependence of the XRD intensity, clearly indicates lower growth rates at higher temperatures. Although the 0.85° ω scan fwhm from the CeO_2 films deposited at 540 °C (Figure 13b) is slightly larger than those previously reported,[46,47,93] this result is impressive considering the low deposition temperature.

XRD ϕ scans demonstrate that the present CeO_2 films have a high degree of in-plane epitaxy with the underlying YSZ (Figure 13c). The fwhm from the ϕ scan of {113} CeO_2, which greatly affects YBCO in-plane alignment and thus the J_c,[104] is 1.65°. Thus, from both the $\theta-2\theta$ and ϕ scans, the orientation of the CeO_2 film on the YSZ substrate has the relationship CeO_2 (001)[$\bar{1}$10]//YSZ (001)[$\bar{1}$10].

AFM studies of the present CeO_2 films give more detail on surface morphology and roughness. Upon increasing the deposition temperature, the grain diameter remains approximately the same (50−110 nm); however, the root-mean-square (rms) film roughness decreases. At low growth temperatures (450 °C; Figure 14a), the rms roughness is ∼15.5 Å. Close observation of the grain particles indicates that the grains are composed of tetragonal-pyramidal shaped hillocks, which are thought to consist of four (111) planes.[93] These hillock formations are not observed in the 540 °C sample (Figure 14b), and the surface of the films is much smoother (rms ∼4.3 Å), most likely owing to the slower growth rates at higher temperatures.

Cross-sectional HREM (Figure 15) shows that a CeO_2 film grown at 540 °C exhibits a high content of single-crystal regions with low defect densities. HREM images and selected-area electron diffraction (Figure 16) confirm the high-quality epitaxial relationship between the CeO_2 and YSZ, as also determined using XRD. The single-crystal-like CeO_2 electron diffraction pattern is characteristic of a high-quality epitaxial film. Owing to the slight lattice mismatch (∼5%), the interface area between the film and substrate contains atomic stacking dislocations having a periodicity of ∼44 Å [(020) layers].[36,47,94] Consistent with the AFM grain size observations, the columnar size remains unchanged; however, the smoothness increases as the deposition temperature is increased. This increased smoothness is doubtless a result of the slower growth rate at higher temperatures, which was determined to decrease from ∼10 Å/min at 450 °C to ∼6.5 Å/min at 540 °C.

Further analysis of the HREM images (Figure 15) reveals that the CeO_2 films are densely packed with no cracks evident either at the interface with the substrate or within the film, consistent with the narrow fwhms of the XRD ϕ and ω scans, and in spite of the columnar microstructure. The single-crystal YSZ substrates, in contrast, are not atomically smooth, and although CeO_2 grows with an abrupt interface on the step planes, crystal plane bending parallel to the surface is observed at the step edges (arrow 1 in Figure 15). Owing to the slight lattice mismatch, stress may build up when the CeO_2 film atomic planes on the lower part of the step attempt to match the neighboring substrate planes, resulting in the observed bending. Crystal plane bending parallel to the surface is also observed at the columnar boundaries of the film (arrow 2 in Figure 15), in a fashion similar to HREM observations on CeO_2 films grown on $SrTiO_3$.[46] Such types of dislocations could alter the XRD ω scan fwhms. When the CeO_2 films are thin, perfectly aligned CeO_2 film portions on the step planes contribute mainly to the narrow portion of the XRD ω-rocking curve, while the broad underlying portion may arise principally from the crystal plane bending of CeO_2 film portions above the substrate steps. With thickening of the CeO_2 films, the existences of atomic plane bending near the columnar boundaries would broaden the XRD ω scan curves, and they would appear as a conventional mosaic, but broader than those of the underlying substrates.

YBCO Film Growth. YBCO films were successfully deposited on the 540 °C MOCVD-derived CeO_2 using a pulsed MOCVD technique, POMBE.[101] XRD $\theta-2\theta$ (Figure 17a) and ω scan (inset, Figure 17a) data show that the YBCO films are (001)-oriented with a high degree of out-of-plane crystallinity. This compares rather well with data for POMBE-derived YBCO (700 °C growth) and MOCVD-derived YSZ (850 °C) bilayer films.[105] A high level of in-plane epitaxy is also revealed by ϕ scan XRD data (Figure 17b). The multilayer therefore has the following heteroepitaxial relationship: (YBCO(001)[010]//CeO_2(001)[$\bar{1}$10]//YSZ(001)[$\bar{1}$10]), with the YBCO rotated 45° in the basal plane of the CeO_2 underlayer. The narrow 1.30° fwhm of the {102} ϕ scan should correlate with high critical current density (J_c).[104] Indeed, four-probe transport measurements reveal a superconducting transition temperature (T_c) of 86.5 K and a J_c of 1.08×10^6 A/cm^2 (Figure 18, plots a and b, respectively). Considering the low deposition temperature of the CeO_2, which simplifies processing and may be critical for multilayer (superconductor−insulator−superconductor) device fabrication, this result represents a significant improvement.

Conclusions

A new series of fluorine-free lanthanide MOCVD precursors has been prepared which exhibit good volatility and lower melting points versus commercial and other previously reported lanthanide sources. The β-ketoiminate ligand is a versatile, multidentate system, producing coordinatively saturated, monomeric lanthanide complexes which are proven here to be excellent MOCVD precursors. Substitution of various alkyl moieties at the keto, imino, and ether sites of the β-ketoiminate ligand offers significant tuning of the melting point and volatility characteristics, facilitating the design of customized lanthanide precursors.

(104) Dimos, D.; Chaaudhari, P.; Mannhart, J. *Phys. Rev. B* **1990**, *41*, 4038−4049.

(105) Kaatz, F. H.; Markworth, P. R.; Dai, J. Y.; Buchholz, D. B.; Liu, X.; Chudzik, M. P.; Belot, J. A.; Kannewurf, C. R.; Marks, T. J.; Chang, R. P. H. *Chem. Vap. Deposition* **1998**, *4*, 99−102.

CeO_2 buffer layer films have been epitaxially deposited on (001) YSZ in the temperature range 450−650 °C by MOCVD using the newly developed $Ce(^tBuMeMe)_3$ precursor. With an increase in deposition temperature, the film growth rate declines while the films tend to be smoother. High-quality epitaxial CeO_2 films can be grown at temperatures as low as 540 °C with smooth surfaces (rms roughness $\sim$ 4.3 Å) and good in-plane ($\Delta\phi = 1.65°$) and out-of plane ($\Delta\omega = 0.85°$) alignment. YBCO films grown on these CeO_2 buffer layers by POMBE are epitaxial and exhibit very good transport properties ($T_c = 86.5$ K, $J_c = 1.08 \times 10^6$ A/cm^2 at 77.4 K). The new precursor has thus proven stable and is attractive for low-temperature growth of CeO_2 buffer layers for coated conductors.

Acknowledgment. We thank the NSF for support of this research through Grant CHE-0076097 and the MRSEC (Materials Research and Engineering Center) Program through the Northwestern Materials Research Center (Grant DMR-0076097).

Supporting Information Available: An X-ray crystallographic file in CIF format containing information for complexes **4**−**7**, **9**, **10**, and **12**. This material is available free of charge via the Internet at http://pubs.acs.org.

IC020299H